AGU PUBLICATIONS

JGR

Journal of Geophysical Research: Atmospheres

RESEARCH ARTICLE
10.1002/2016JD025016

Key Points:
- Estimation of mineral dust direct radiative forcing
- Comparison of two different radiative transfer models (GAME and Two-stream)
- Impact of radiative transfer model spectral resolutions

Correspondence to:
R. Barragan,
ruben.barragan@tsc.upc.edu

Citation:
Barragan, R., S. Romano, M. Sicard, P. Burlizzi, M. R. Perrone, and A. Comeron (2016), Estimation of mineral dust direct radiative forcing at the European Aerosol Research Lidar NETwork site of Lecce, Italy, during the ChArMEx/ADRIMED summer 2013 campaign: Impact of radiative transfer model spectral resolutions, *J. Geophys. Res. Atmos.*, *121*, 10,237–10,261, doi:10.1002/2016JD025016.

Received 3 MAR 2016
Accepted 7 AUG 2016
Accepted article online 10 AUG 2016
Published online 15 SEP 2016

Estimation of mineral dust direct radiative forcing at the European Aerosol Research Lidar NETwork site of Lecce, Italy, during the ChArMEx/ADRIMED summer 2013 campaign: Impact of radiative transfer model spectral resolutions

Ruben Barragan[1,2], Salvatore Romano[3], Michaël Sicard[1,2], Pasquale Burlizzi[3], Maria Rita Perrone[3], and Adolfo Comeron[1]

[1]Remote Sensing Laboratory, Universitat Politècnica de Catalunya, Barcelona, Spain, [2]Ciències i Tecnologies de l'Espai, Centre de Recerca de l'Aeronàutica i de l'Espai/Institut d'Estudis Espacials de Catalunya, Universitat Politècnica de Catalunya, Barcelona, Spain, [3]Dipartimento di Matematica e Fisica, Università del Salento, Lecce, Italy

Abstract A field campaign took place in the western and central Mediterranean basin on June–July 2013 in the framework of the ChArMEx (Chemistry-Aerosol Mediterranean Experiment, http://charmex.lsce.ipsl.fr/)/ADRIMED (Aerosol Direct Radiative Impact on the regional climate in the MEDiterranean region, http://adrimed.sedoo.fr/) project to characterize the aerosol direct radiative forcing (DRF) over the Mediterranean. This work focuses on the aerosol DRF estimations at Lecce (40.33°N; 18.11°E; 30 m above sea level) during the Saharan dust outbreak that affected southern Italy from 20 to 24 June 2013. The Global Atmospheric Model (GAME) and the Two-Stream (TS) model were used to calculate the instantaneous aerosol DRF in the short-wave (SW) and long-wave (LW) spectral ranges, at the surface and at the top of the atmosphere (TOA). The main differences between the two models were due to the different numerical methods to solve the radiative transfer (RT) equations and to the more detailed spectral resolution of GAME compared to that of TS. 167 and 115 subbands were used by GAME in the 0.3–4 and 4–37 μm spectral ranges, respectively. Conversely, the TS model used 8 and 11 subbands in the same spectral ranges, respectively. We found on 22 June that the SW-DRFs from the two models were in good agreement, both at the TOA and at the surface. The instantaneous SW-DRFs at the surface and at the TOA varied from −50 to −34 W m^{-2} and from −6 to +8 W m^{-2}, respectively, while the surface and TOA LW-DRFs ranged between +3.5 and +8.0 W m^{-2} and between +1.7 and +6.9 W m^{-2}, respectively. In particular, both models provided positive TOA SW-DRFs at solar zenith angles smaller than 25° because of the mixing of the desert dust with anthropogenic pollution during its transport to the study site. In contrast, the TS model overestimated the GAME LW-DRF up to about 5 and 7.5 times at the surface and at the TOA, respectively, when the dust particle contribution was largest. The low spectral resolution of the real (n) and imaginary (k) refractive index values was mainly responsible for the LW-DRF overestimates of the TS model. However, we found that the "optimization" of the n and k values at 8.75 and 11.5 μm was sufficient in this study to obtain a satisfactory agreement between the LW-DRFs from the two models, both at the TOA and at the surface. The impact of the spectral dependence of the water vapor absorption coefficients on the estimation of the flux without aerosol has also been addressed. Paper results did not reveal any significant impact due to the different numerical methods used by the two models to solve the RT equations.

1. Introduction

The Mediterranean basin is located at the crossroads of air masses carrying both natural (e.g., desert particles, sea salt, and volcanic ashes) and anthropogenic (e.g., black carbon and sulfate) aerosols from continental and ocean sources [*Lelieveld et al.*, 2002]. Atmospheric aerosols greatly affect the regional hydrological cycle, cloud cover, precipitations, and the atmospheric radiative budget in the Mediterranean region. The aerosol impact on the radiative budget at the scale of the Mediterranean basin is assessed by regional climate models [*Nabat et al.*, 2015], which do not properly take into account the possible radiative influence of the different Mediterranean aerosols, as recently mentioned by *Mallet et al.* [2006]. Aerosol radiative forcing estimates obtained with one-dimensional (1-D) radiative transfer models (RTM) have commonly been used to constrain and/or validate regional climate models. Many 1-D RTMs have been reported in the literature, and some of

them are available online as open-source codes. SBDART [*Ricchiazzi et al*., 1998], Streamer [*Key and Schweiger*, 1998], MODTRAN [*Berk et al*., 2006], and libRadtran [*Mayer and Kylling*, 2005] represent some of the online available RTMs, widely accepted and used by the scientific community. The 1-D RTMs are also often used to locally estimate the aerosol radiative forcing under clear-sky or cloudy conditions. Many studies were performed to investigate the aerosol direct radiative effects at selected Mediterranean sites [e.g., *Formenti et al*., 2002; *Meloni et al*., 2003, 2015; *Roger et al*., 2006; *Mallet et al*., 2006; *Perrone et al*., 2012; *Sicard et al*., 2012, 2014a; *Román et al*., 2013; *Bilbao et al*., 2014; *Mallet et al*., 2016; *Romano et al*., 2016]. Most of the aerosol optical properties required in RTMs can be retrieved from experimental measurements in the short-wave (SW) spectral range. On the contrary, the aerosol optical properties in the long-wave (LW) spectral range have to be taken from look-up tables or calculated by using light scattering codes [*Sicard et al*., 2014a], since the current remote sensing technologies do not allow retrieving them. The atmospheric parameters not related to the aerosols (e.g., concentration of absorbing gases, relative humidity profile, surface albedo, and temperature) also may significantly influence the estimation of the radiative fluxes in the SW and in the LW spectral range, respectively. Therefore, many sources of uncertainty can affect the determination of the aerosol direct radiative forcing. SW and LW fluxes simulated by RTMs are commonly compared with the corresponding ones measured at the bottom of the atmosphere (BOA) and at the top of the atmosphere (TOA) to test the performance of RTMs and estimate the accuracy of the calculated aerosol direct radiative effect [e.g., *Romano et al*., 2016].

In the context of the Chemistry-Aerosol Mediterranean Experiment (ChArMEx; http://charmex.lsce.ipsl.fr)/ Aerosol Direct Radiative Forcing on the Mediterranean Climate (ADRIMED, http://adrimed.sedoo.fr/) project [*Dulac*, 2014], intensive measurements of the aerosol radiative properties were carried out in the western and central Mediterranean basin during the summer 2013 field campaign [*Mallet et al*., 2016]. In particular, continuous measurements of the SW and LW radiative fluxes at the surface were carried out at the Mathematics and Physics Department of the Salento University (Lecce, Italy) during the moderate Saharan dust outbreak that affected the Mediterranean basin from 15 up to the 25 June 2013 [*Barragan et al*., 2015]. In this work, we have investigated the aerosol SW and LW direct radiative forcing (DRF) at the BOA and at the TOA in Lecce, from 20 to 24 June 2013. To this end, two radiative transfer models, the Global Atmospheric Model (GAME) [*Dubuisson et al*., 2004, 2006] and the Two-Stream model [*Tafuro et al*., 2007; *Perrone and Bergamo*, 2011; *Perrone et al*., 2012], were used. The capability of both models to reproduce the experimental flux measurements and the dependence of the aerosol DRF estimates on the used RTM have mainly been investigated. Note that the two models use different numerical procedures to calculate the radiative field and a different spectral resolution for the aerosol optical properties. Therefore, the dependence of the flux and the aerosol DRF estimates on the used RTM has mainly been investigated by a case study analysis and sensitivity tests. Results on the methodology used to decrease the differences between the outputs from the two models have also been provided in the paper. Some details on the main objectives of the ChArMEx/ADRIMED summer 2013 field campaign and the used instrumentation are presented in section 2. A detailed description of both models is reported in section 3. The investigated mineral dust intrusion is described in section 4. The main results related to the radiative flux and aerosol DRF estimates from the two models, in addition to the adopted methodology to decrease the differences between the two models, are presented and discussed in section 5. Summary and conclusions are in section 6.

2. The ChArMEx/ADRIMED Field Campaign, Monitoring Site and Instrumentation

2.1. Overview of the ChArMEx/ADRIMED Field Campaign Objectives

The main goal of the ChArMEx international program is the scientific assessment of the present and future state of the atmospheric environment in the Mediterranean basin and its impact on the regional climate, air quality, and marine biogeochemistry [*Dulac*, 2014]. To this end, the ChArMEx observation strategy is based on long, enhanced, and special observation periods of increasing intensity. ADRIMED is a French 4 year project which has the objective of establishing an innovative database of the aerosol physical, chemical, and optical properties in order to (1) estimate more precisely the 1-D local direct radiative forcing, (2) constrain 3-D regional climate models, and (3) investigate how the changes of the radiative budget (especially at the sea surface) due to the aerosol particles affect the sea surface evaporation fluxes and the Mediterranean hydrological cycle during the dry season [*Mallet et al*., 2016]. The largest ChArMEx special observation period (SOP) in the western and central Mediterranean basin was carried out in conjunction with the ADRIMED project (SOP-1a). It took place between 12 June and 5 July 2013 at seven different sites of the western and central

Mediterranean. Balloon and aircraft measurements were performed during the campaign, in addition to ground-based measurements. More details about the campaign can be found in *Mallet et al*. [2016]. Some EARLINET/ACTRIS (European Aerosol Research Lidar NETwork/Aerosols, Clouds, and Trace gases Research InfraStructure Network, http://www.actris.eu/) [*Pappalardo et al*., 2014] lidar stations operating in Spain and Italy gave support to the measurements. In particular, the EARLINET station of the Salento University in Lecce, Italy, performed continuous daytime lidar measurements, as well as SW and LW radiative flux measurements at the surface during the moderate Saharan dust outbreak that affected the Mediterranean basin from west to east, from 15 to 25 June 2013.

2.2. Monitoring Site and Instrumentation

The monitoring station of the Mathematics and Physics Department of the Salento University is located on a flat peninsular area (40.33°N; 18.11°E; 30 m asl, above sea level) of southeastern Italy, 6 km away from the town of Lecce (~95,000 inhabitants) and ~20 km away from both the Ionic and Adriatic Seas. The study site can be classified as rural background, accordingly to *Larssen et al*. [1999]. In addition, it can be considered as representative of coastal sites of the central Mediterranean away from large sources of local pollution, according to *Perrone et al*. [2014a].

Two Kipp & Zonen pyranometers (CMP 21 model) and two Kipp & Zonen pyrgeometers (CGR 3 model) were used to measure the downward and upward irradiance at the surface in the SW (0.31–2.8 μm) and in the LW (4.5–42 μm) spectral range, respectively. The CMP 21 pyranometer is classified as "secondary standard instrument," which represents the best pyranometer class according to the ISO 9060 standard adopted by the World Meteorological Organization. The CMP 21 pyranometer and the CGR 3 pyrgeometer have a total uncertainty of 2 and 3%, respectively, taking into account temperature, calibration, and cosine error of the devices [*Yan et al*., 2011]. The pyranometers and the pyrgeometers were located at 1.5 m above ground level so as to have the horizon free of significant obstacles. The radiative flux values were collected with a temporal resolution of 2 min.

Measurements from the AERONET (Aerosol Robotic Network; http://aeronet.gsfc.nasa.gov/) [*Holben et al*., 1998] Sun/sky photometer operating at the study site since 2003 were used to determine the columnar aerosol properties. The CIMEL CE 318-4 photometer is a solar-powered weather hardy robotically pointed Sun/sky spectral radiometer, which performs direct solar flux and water vapor measurements at 340, 380, 440, 675, 870, 940, and 1020 nm, and diffuse-sky flux measurements at 440, 675, 870, and 1020 nm. Several aerosol properties are retrieved by an inversion algorithm based on both spectral direct Sun and diffuse-sky radiance measurements [*Dubovik et al*., 2006]. A discussion on the accuracy of the AERONET aerosol products is reported in *Dubovik et al*. [2000, 2002], especially for the aerosol radiative properties used in this study, namely, the aerosol optical depth (AOD), the single scattering albedo (SSA), and the asymmetry factor. Recently, *Sicard et al*. [2016] made a nice summary of the accuracy of most of AERONET products.

Lidar measurements were performed in Lecce by using the system identified as UNILE (UNIversity of LEcce) lidar, which operates within EARLINET since 2000 [*De Tomasi et al*., 2006]. The UNILE lidar system is nowadays composed of a 30 Hz Nd:YAG laser operating at its fundamental wavelength (1064 nm) and the second and third harmonics at 532 and 355 nm, respectively. The linear polarized laser pulses are about 10 ns long with maximum energy per pulse of 1600, 790, and 530 mJ at 1064, 532, and 355 nm, respectively. In addition to the elastic channels, the system is equipped with the N_2- and H_2O-Raman channels, as well as a depolarization channel. Lidar products are profiles of backscatter coefficients at 1064, 532, and 355 nm and the particle depolarization ratio at 355 nm during daytime. The vertical profiles of extinction and backscatter coefficients at 1064, 532, and 355 nm, particle depolarization ratio at 355 nm, and water vapor mixing ratio are retrieved from nighttime lidar measurements. In this study, only daytime lidar data were considered. During daytime, the elastic algorithm uses a height-independent lidar ratio (LR) value, i.e., the ratio between the extinction and the backscatter coefficients. In particular, the LR value is chosen in order to obtain from the integral of the extinction coefficient profiles AOD values equal to the ones retrieved from Sun/sky photometer measurements collocated in space and time [*Perrone et al*., 2014b].

3. Description of the Radiative Transfer Models

The GAME and the Two-Stream RTMs have been used to simulate the SW and LW radiative fluxes with and without aerosol and, hence, to determine the aerosol DRF at the BOA and at the TOA during the investigated

African dust event. The aerosol DRF, which accounts for changes in the radiation levels due to the atmospheric aerosols, is defined as the difference between the net fluxes with and without aerosol:

$$\mathrm{DRF}_{\mathrm{BOA}} = \left(F^{\mathrm{DN}}_{\mathrm{BOA}} - F^{\mathrm{UP}}_{\mathrm{BOA}}\right) - \left(F^{\mathrm{DN,0}}_{\mathrm{BOA}} - F^{\mathrm{UP,0}}_{\mathrm{BOA}}\right) \quad (1)$$

$$\begin{aligned}\mathrm{DRF}_{\mathrm{TOA}} &= \left(F^{\mathrm{DN}}_{\mathrm{TOA}} - F^{\mathrm{UP}}_{\mathrm{TOA}}\right) - \left(F^{\mathrm{DN,0}}_{\mathrm{TOA}} - F^{\mathrm{UP,0}}_{\mathrm{TOA}}\right) \\ &= F^{\mathrm{UP,0}}_{\mathrm{TOA}} - F^{\mathrm{UP}}_{\mathrm{TOA}}\end{aligned} \quad (2)$$

where F^{DN} and F^{UP} are the downward and upward fluxes with aerosol, while $F^{\mathrm{DN,0}}$ and $F^{\mathrm{UP,0}}$ are the downward and upward fluxes without aerosol, respectively.

3.1. The GAME Radiative Transfer Model

The GAME code is widely described by *Dubuisson et al*. [2004, 2006] and recently in the LW spectral range by *Sicard et al*. [2014a]. The GAME code allows calculating the solar and thermal infrared fluxes in two adjustable spectral ranges that were fixed exactly equal to those of Two-Stream (TS): SW (0.3–4 μm) and LW (4–37 μm), at the boundary of plane and homogenous atmospheric layers by using the discrete ordinates method [*Stamnes et al*., 1988]. Note that the GAME code has a variable spectral sampling in the SW (depending on the spectral range considered and a wave number of 100 or 400 cm^{-1}) and a fixed spectral sampling (115 values) in the infrared spectral range. About the vertical resolution of the model, 40 vertical levels are used, in the LW version, between ground and 100 km height with a resolution of 1 km from the surface to 25 km, 2.5 km between 25 and 50 km, 5 km from 50 to 60 km, and 20 km between 80 and 100 km. In the SW version, 18 vertical levels are used between ground and 20 km height with a resolution of 5 m from the surface to 10 m, 10 m between 10 and 50 m, 50 m between 50 and 100 m, 100 m between 100 and 200 m, 200 m between 200 and 1 km, 1 km between 1 and 2 km, 2 km between 2 and 10 km, and 10 km between 10 and 20 km. One of its main specificities is the representation of the LW aerosol scattering, which is often neglected in regional and global climate models in spite of its effect on the LW radiative forcing [*Sicard et al*., 2014a].

3.2. The Two-Stream Radiative Transfer Model

The Two-Stream RTM used in this study is widely described in *Tafuro et al*. [2007], *Perrone and Bergamo* [2011], and *Perrone et al*. [2012]. It uses the two-stream approximation [*Meador and Weaver*, 1980] to solve the radiative transfer equation and to simulate the SW and LW radiative fluxes at the boundary of 20 homogeneous plane-parallel layers from the surface up to 25 km. In particular, 10 layers (with a resolution of 500 m) are placed below 5 km altitude, to better evaluate the effects of the lower tropospheric aerosols. In this study, the radiative fluxes were determined in the SW (0.3–4 μm) and in the LW (4–37 μm) domains. In particular, 8 SW and 11 LW subbands were considered to properly account for the spectral dependence of the atmospheric particle properties.

3.3. Main Features of the Two Models and Input Parameters

The procedure to calculate the radiative field for a given distribution of the aerosol optical properties is the heart of all RTMs [*Mayer and Kylling*, 2005]. The calculation procedure ranges from a variety of parameterizations and approximations to sophisticated and accurate solutions of the 3-D radiative transfer equation. Note that the two-stream approximation [*Meador and Weaver*, 1980], which is used in the Two-Stream model, is one of the simplest techniques to solve the radiative transfer equation. The discrete ordinate method used in GAME is expected to be more accurate than the two-stream approximation.

Table 1 provides the list of the main parameters used as inputs of the two RTMs in the SW and LW spectral ranges, respectively. The used broadband surface albedo values were experimentally determined as the ratio of the SW upward irradiance to the corresponding SW downward irradiance, measured by the pyranometers at the surface [*Manninen et al*., 2012]. The LW emissivity was calculated by averaging all the values provided by the CERES (Clouds and Earth's Radiant Energy System) SSF (Single Scanner Footprint) Level 2 data set (http://ceres.larc.nasa.gov/) for an area of 0.5° latitude by 0.5° longitude around the study site. The time-dependent refractive indices from AERONET Sun/sky photometer measurements were used in the SW spectral range, while the time-independent refractive indices for mineral dust from *Krekov* [1993] were used in the LW spectral range. Input data include also the columnar aerosol volume size distribution from AERONET retrievals. Air density, atmospheric pressure, and water vapor mixing ratio values at the surface were provided by a local meteorological station. The skin surface temperature (T_S) values were experimentally

Table 1. Overview of the GAME and the Two-Stream Model Properties[a]

		Short Wave		Long Wave	
Parameters		GAME	Two-Stream	GAME	Two-Stream
Spectral range		0.3–4 μm	0.3–4 μm	4–37 μm	4–37 μm
Number of subbands		167	8	115	11
Meteo parameters	At the surface	Local data	Local data	Local data	Local data
	<20 km	Radiosounding	Radiosounding	Radiosounding	Radiosounding
	>20 km	US standard atmosphere	US standard atmosphere	US standard atmosphere	US standard atmosphere
Main gases parameters	Concentration profile	US standard atmosphere	US standard atmosphere	US standard atmosphere	US standard atmosphere
	Absorption coefficients	HITRAN	LOWTRAN 5	HITRAN	LOWTRAN 5
Surface parameters	Surface albedo	Ground-based measurements	Ground-based measurements		
	LW emissivity			CERES	CERES
Aerosol parameters	Vertical distribution	Lidar	Lidar	Lidar	Lidar
	Size distribution	AERONET	AERONET	AERONET	AERONET
	Fine and coarse mode radius	AERONET	AERONET	AERONET	AERONET
	Refractive index	AERONET	AERONET	*Krekov* [1993]	*Krekov* [1993]

[a]Meteo parameters include atmospheric pressure, air temperature, air density, and relative humidity.

calculated from the downward and upward long-wave irradiances measured at the surface by the following relation [*Wang et al*., 2005]:

$$\text{LW-}F^{\text{UP}} = \varepsilon\,\sigma\,T_S^{\,4} + (1-\varepsilon)\,\text{LW-}F^{\text{DN}} \tag{3}$$

where ε represents the surface LW emissivity (0.015 on 20 and 21 June and 0.014 on 22 and 24 June) and σ is the Stefan-Boltzmann's constant.

The temperature (T), relative humidity (RH), and pressure (P) vertical profiles were obtained from radio sounding measurements performed at the meteorological station of Brindisi (Italy) that is about 40 km northwest of the Lecce monitoring station. The T, RH, and P profiles were interpolated to the vertical resolution of the models, up to 20 km of altitude. Summer and midlatitudes standard atmosphere data provided by the Air Force Geophysics Laboratory (AFGL) [*Anderson et al*., 1986] were then used above 20 km of altitude. The water vapor mixing ratio, defined as the ratio of the mass of water vapor to the mass of dry air, was calculated from the radio sounding RH, P, and T values, according to *Wagner and Pruß* [2002].

The transmission function (T_υ) of the atmospheric gases for a spectral interval υ and an atmospheric layer at pressure P and temperature T was approximated by an exponential summation over a limited number N of absorption classes as [*Sicard et al*., 2014a]

$$T_\upsilon(P,T) = \sum_{i=1}^{N} a_i e^{-k_i(P,T)u(P,T)} \tag{4}$$

where u represents the absorber amount and a_i represents the probability associated to the mean absorption coefficient k_i for each absorption class i. The a_i and k_i values were retrieved from the HITRAN (HIgh-resolution TRANsmission molecular absorption) spectroscopic database and the Line-by-Line DOM code [*Dubuisson et al*., 1996] for GAME and from the LOWTRAN (LOW resolution TRANsmission model) 5 database for the Two-Stream model.

The aerosol vertical distribution was assessed in both models from the vertical profiles of the backscatter coefficient at 532 nm (β_{532}), retrieved from the UNILE lidar measurements.

Observe from Table 1 that the different spectral resolution adopted in the two models can represent a source of discrepancy in the provided values of the simulated radiative fluxes and, consequently, aerosol DRFs. In fact, *Hatzianastassiou et al*. [2007] highlighted the importance of performing detailed spectral computations to provide reliable estimates of the aerosol's climate role. In particular, they demonstrated by sensitivity tests that very large differences (up to 300%) could be found between aerosol DRFs computed using detailed spectral and spectrally averaged aerosol optical properties. An additional source of discrepancy in the data provided by the two models could be due to the fact that the HITRAN spectroscopic database is used in GAME for the atmospheric gases, while the LOWTRAN 5 database is used in the Two-Stream model. Note that the LOWTRAN 5 database may underestimate the near-infrared water vapor absorption by about 10%, according to *Halthore et al*. [2005].

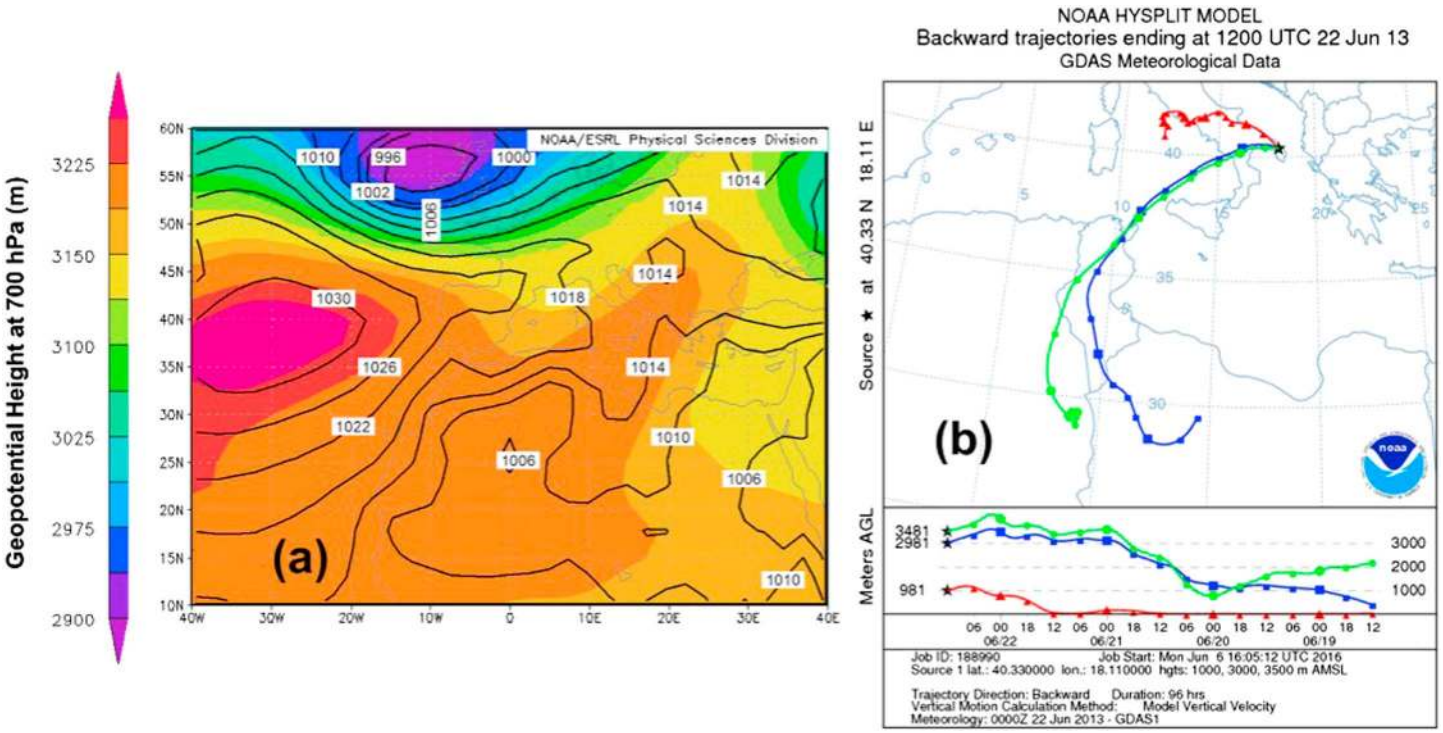

Figure 1. (a) Geopotential height at 700 hPa (shadow) and pressure at sea level in hectopascals (black lines) for 22 June 2013. (b) Pathways of the 4 day analytical back trajectories at 1000 (red), 3000 (blue), and 3500 m (green) above sea level reaching the study site at 12:00 UTC on 22 June 2013 from the HYSPLIT model.

4. Characterization of the 20–24 June 2013 Dust Event

The SOP-1a campaign was mostly characterized by a moderate aerosol loading [*Mallet et al*., 2016]. The dust plume detected during SOP-1a moved from southern Spain on 15 June to southeastern Italy on 22 June. The northwestern Mediterranean area was on 15 June under the influence of a large pressure ridge at 700 hPa, generating a westerly to southwesterly flow over Spain and southern France, which reinforced on 16 June advecting air masses with large concentrations of dust aerosols, as shown by SEVERI AOD for that day [*Barragan et al*., 2015]. A low-pressure system moved from Great Britain toward the Gulf of Biscay and then the Iberian Peninsula between 17 and 20 June, leading to veering winds that became southerly over the northwestern Mediterranean. After 20 June, this low-pressure system moved eastward, generating a trough located between France and Italy and inducing a waving westerly flow over the northwestern Mediterranean, as the synoptic conditions shown in Figure 1a clearly reveal. The geopotential height at 700 hPa and the sea level atmospheric pressure for 22 June, provided by the NOAA-ESRL Physical Science Division (http://www.esrl.noaa.gov/psd/), are shown in Figure 1a. The aerosol loading over the western Mediterranean basin decreased between 21 and 24 June, while the transport of dust increased over the central basin, as a consequence of the synoptic conditions over the Mediterranean. Figure 1b shows the 96 h analytical back trajectories of the air masses that reached the monitoring site at 12:00 UTC on 22 June at 1000, 3000, and 3500 m asl from the HYSPLIT (HYbrid Single Particle Lagrangian Integrated Trajectory; http://ready.arl.noaa.gov) model [*Stein et al*., 2015]. Note that lidar measurements performed at the study site on 22 June (not shown) revealed that the dust load extended up to about 5000 m asl. Figure 1b shows that the air masses which reached the monitoring site at 3000 m asl were originated over arid regions of Tunisia and Libya at low altitudes. Figure 2 shows the temporal evolution of the daily AOD at 550 nm over the Mediterranean basin from MSG-SEVIRI, from 19 to 24 June, to support the previous comments. As shown in Figure 2, the eastward transport of the dust plume is clearly visible during the studied period, and the presence of the dust plume over the monitoring site of this study was particularly evident on 22 and 23 June, which represented the days most affected by the desert dust advection. Figure 3 shows the hourly mean values of the (a) SW and (b) LW downward radiative flux (SW- and LW-F^{DN}, respectively), and of the (c) relative humidity (RH), (d) water vapor pressure (WVP), and (e) air temperature (T) from 20 to 24 June, to provide an overview of the local

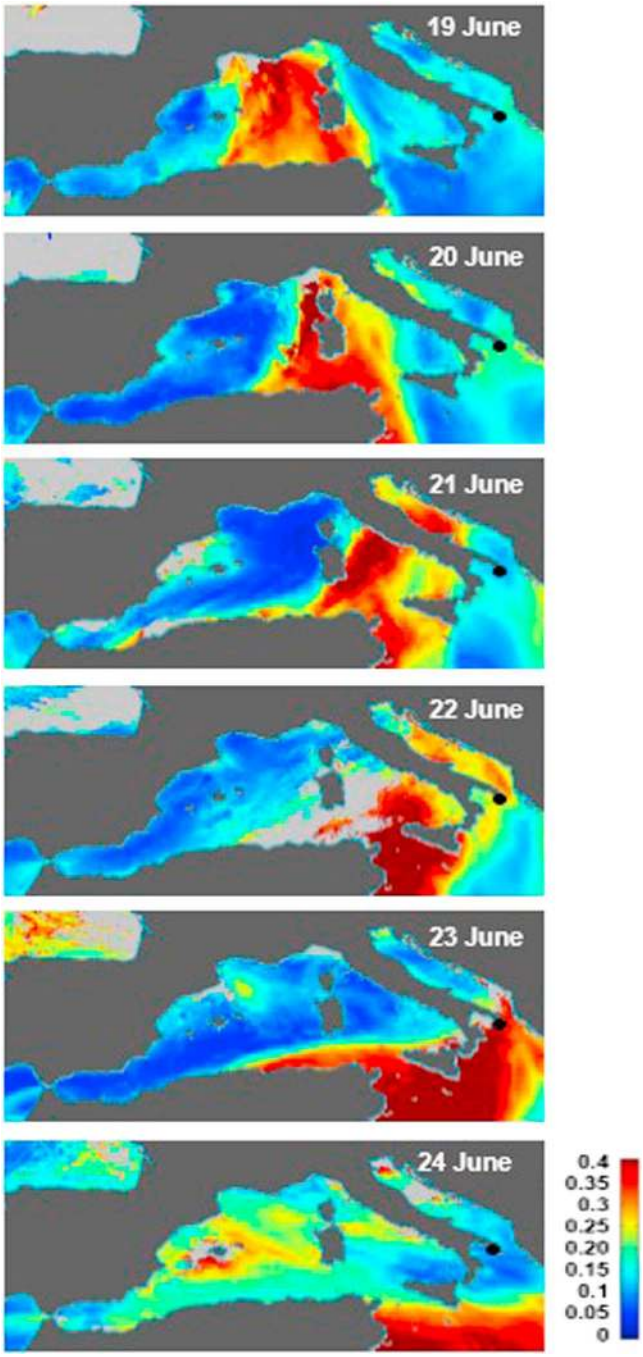

Figure 2. Color map of the aerosol optical depth (at 550 nm) daily mean values over the Mediterranean Sea from the MSG-SEVIRI instrument—ICARE Thematic Center (http://www.icare.univ-lille1.fr/), from 19 to 24 June 2013. The black point indicates the position of the site analyzed in this study, Lecce (Italy).

meteorological conditions during the analyzed period. The multipeaks structure of the SW-F^{DN} time evolution on 23 June (Figure 3a) reveals that it was a cloudy day. In fact, the SW-F^{DN} time evolution was characterized by a typical clear-sky daily cycle on 20–22 and 24 June reaching maximum values between 940 and 970 W m^{-2} around midday. By comparing Figures 3b and 3e, one can observe the significant correlation between the LW-F^{DN} values and the corresponding T values: both parameters show an increasing trend from early morning to midday and a decreasing trend from midday to the final hours of the day. Then, note from Figure 3b that the highest LW-F^{DN} value (430 W m^{-2}) was found at 14:00 UTC on 23 June, the cloudiest day during the analyzed period. It was associated with a peak value of T (32.6°C) and minimum values of SW-F^{DN}, RH, and WVP (109 W m^{-2}, 27%, and 3.2 mbar, respectively). *Bilbao and De Miguel* [2007] indicated that the daily time evolution of meteorological parameters and radiative fluxes is on average characterized by a multipeak structure on cloudy days, in agreement with the results of this study referred to 23 June (Figure 3). Figure 3 allows also estimating the effect of the desert dust advection on the irradiance and the meteorological parameters that occurred on 22 June. Figure 2 shows that the AOD at 550 nm increased significantly at the monitoring site of this study from 21 to 22 June. Then, Figure 3 reveals that the desert dust advection was responsible from midday of 21 June to midday of 22 June for a SW-F^{DN} decrease of 30 W m^{-2} (3%), a LW-F^{DN} increase of 5 W m^{-2} (1.5%), a RH increase of 18% (48%), a WVP increase of 2.1 mbar (47%), and a T decrease of 1.6°C (5%). Note that AERONET and lidar measurements were not performed on 23 June since it was a cloudy day, as shown in Figure 3. Figure 4 shows the temporal evolution of the instantaneous values of (a) the AOD at 440 and 1020 nm (open black triangles and dots, respectively), (b) the Ångström exponents calculated at the wavelength pair 440–870 nm ($AE_{440-870}$) (open black dots), and (c) the SSA at 440 and 1020 nm (open black triangles and dots, respectively), all retrieved from AERONET Sun/sky photometer measurements (Level 2.0) at the monitoring site. Full symbols and error bars in Figure 4 represent the daily mean values and the corresponding ±1 standard deviations, respectively. The daily

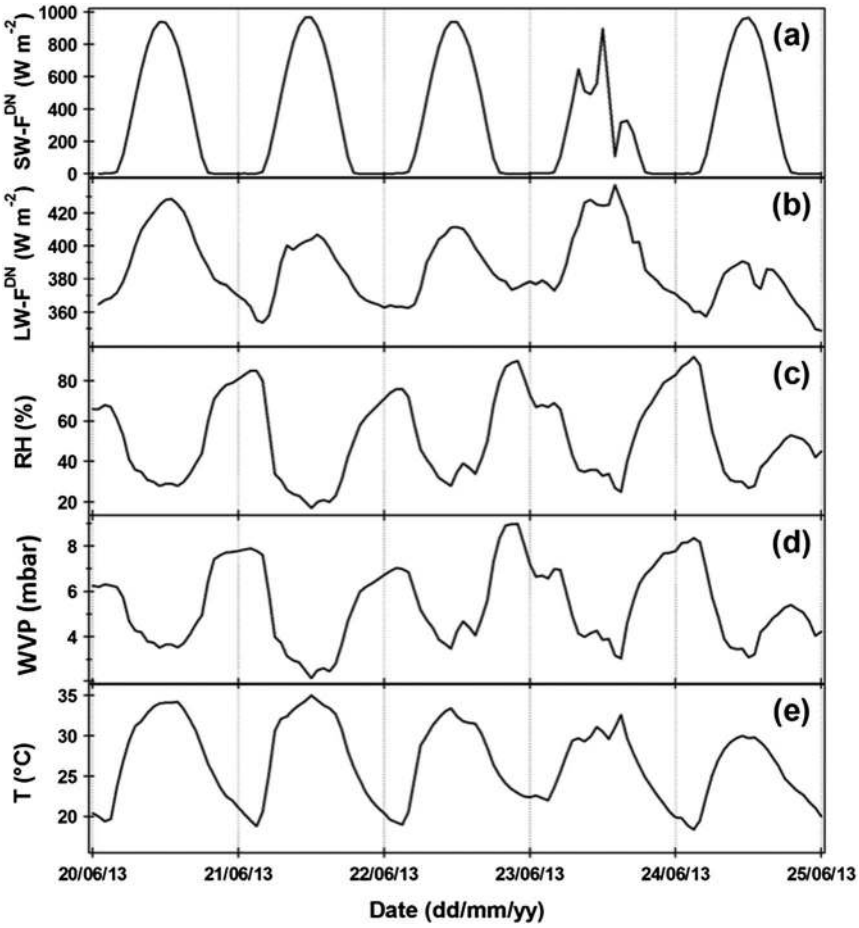

Figure 3. Temporal evolution of the hourly mean values of (a) short-wave downward radiative flux (SW-F^{DN}), (b) long-wave downward radiative flux (LW-F^{DN}), (c) relative humidity (RH), (d) water vapor pressure (WVP), and (e) air temperature (T) in Lecce (Italy), from 20 to 24 June 2013.

mean value of the AOD at 440 nm (AOD_{440}) increased from 0.19 on 20 June up to 0.25 on 22 June because of the large advection of desert dust (Figure 4a). Consequently, the $AE_{440-870}$ daily mean value, which was equal to 1.92 on 20 June, decreased up to 0.90 on 22 June (Figure 4b). Note that a combination of large AODs with small AE values may indicate a significant contribution of coarse mode particles, as mineral dust, to the aerosol load [e.g., *Cachorro et al*., 2008]. The SSA, which represents the ratio between scattering and extinction coefficient, shows a particular spectral behavior during a desert dust intrusion. Some works performed at Mediterranean sites [e.g., *Valenzuela et al*., 2012; *Romano et al*., 2016; *Sicard et al*., 2016] found that the SSA exhibited a substantial increase from 440 to 675 nm and, then, a slight increase as a function of the wavelength on dusty days. Accordingly, we have found that the SSA daily mean values were equal to 0.892, 0.906, 0.912, and 0.921 at 440, 675, 870, and 1020 nm, respectively, on 22 June (dusty day). Conversely, the SSA values decreased with the wavelength increase on 20 June (Figure 4c), which likely represented a day weakly affected by desert dust. In particular, the SSA daily mean value decreased from 0.944 at 440 nm to 0.885 at 1020 nm on 20 June (Figure 4c, full symbols). Note that the SSA spectral behavior of 20 June is typical of urban/industrial or mixed aerosols, according to *Russell et al*. [2010].

5. Results

5.1. Comparison of Modeled and Experimental Radiative Fluxes

The SW and LW radiative fluxes monitored at Lecce from 20 to 24 June 2013 during the ChArMEx/ADRIMED campaign have been compared with the corresponding fluxes modeled by the GAME and the Two-Stream

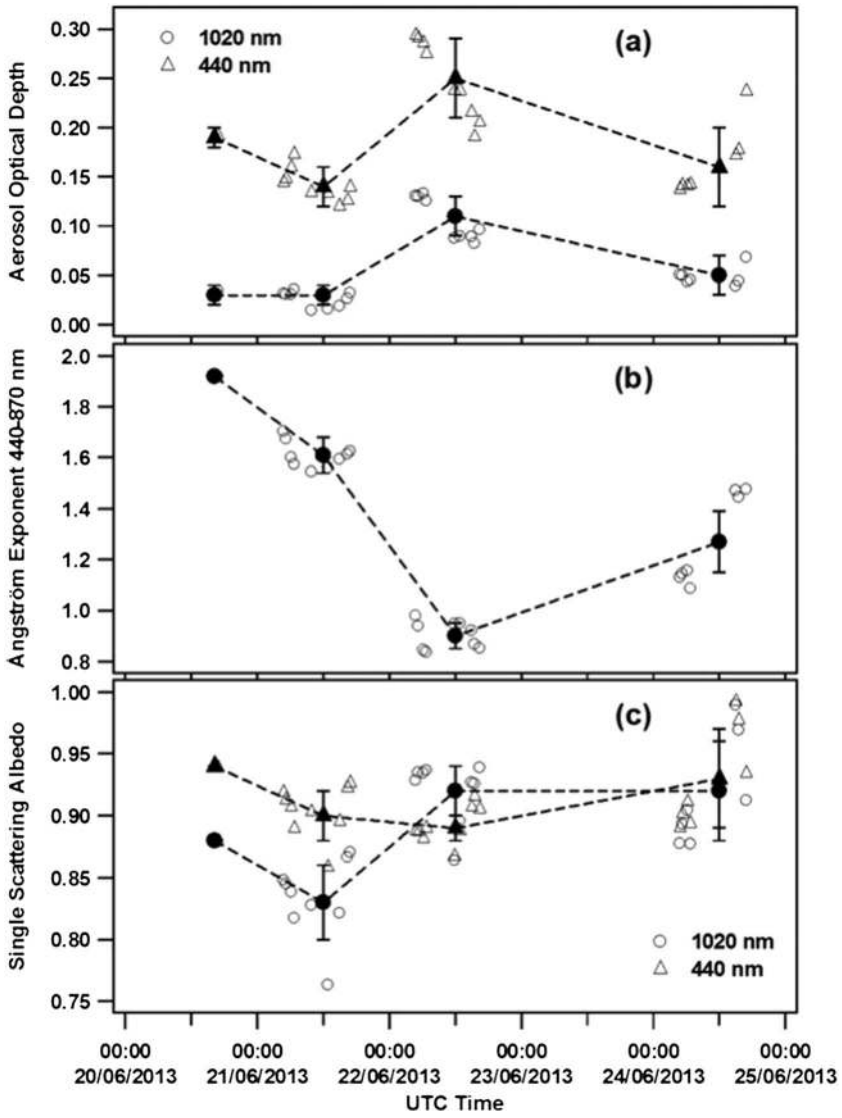

Figure 4. Temporal evolution of the instantaneous (a) aerosol optical depth values at 440 nm (open triangles) and 1020 nm (open dots), (b) Ångström exponents at the wavelength pair 440–870 nm (open dots), and (c) single scattering albedo values at 440 nm (open triangles) and 1020 nm (open dots), from AERONET Sun/sky photometer measurements (level 2.0 data) in Lecce (Italy), from 20 to 24 June 2013. The full symbols and the error bars represent the daily mean values and the corresponding standard deviations, respectively.

code, respectively, to obtain a first estimate of the accuracy of both RTMs. Model simulations have only been performed at the times in which collocated in space and time lidar and AERONET Sun/sky photometer measurements were available. Therefore, 21 values of SW and LW radiative fluxes were simulated during the four analyzed days (see Table 2). Figures 5a and 5b show for comparison the calculated SW downward and upward fluxes, respectively, versus the corresponding measured fluxes at the surface. More specifically, black triangles and grey dots in Figure 5 represent the GAME and the Two-Stream calculated fluxes, respectively. The dashed grey line in Figure 5 shows the 1:1 line. The measured radiative fluxes plotted in Figure 5 were calculated by averaging the measured flux values over a 10 min interval centered at the mean time of the lidar signals averaged to obtain a single profile. Error bars in Figure 5 represent ±1 standard deviation (SD) of the measured flux mean values. Figure 5 reveals that both the GAME (black triangles) and the Two-Stream (grey dots) simulated SW fluxes were in good agreement with the corresponding experimental values, being the square of the linear correlation coefficient $R^2 = 0.99$. Note also that the GAME and the Two-Stream SW flux values on average slightly underestimated and overestimated, respectively, the

Table 2. Instantaneous, Clear-Sky, Short-Wave (SW), and Long-Wave (LW) Direct Radiative Forcing (DRF) at the Bottom of the Atmosphere (BOA) and at the Top of the Atmosphere (TOA) Simulated by GAME (G) and Two-Stream (TS) Radiative Transfer Model for 21 Selected Times/Days of June 2013[a]

					BOA SW-DRF ($W\,m^{-2}$)		TOA SW-DRF ($W\,m^{-2}$)		BOA LW-DRF ($W\,m^{-2}$)		TOA LW-DRF ($W\,m^{-2}$)	
Day	SZA (deg)	AOD	SSA	SA	G	TS	G	TS	G	TS (O-TS)	G	TS (O-TS)
20	53	0.19	0.94	0.22	−14	−15	−6	−6	3.1	2.2 (1.9)	1.4	1.6 (1.6)
20	59	0.19	0.94	0.23	−14	−15	−6	−6	2.9	2.3 (2.0)	1.1	1.4 (1.4)
20	64	0.19	0.94	0.25	−14	−15	−8	−8	2.7	2.4 (1.8)	0.8	1.3 (1.4)
20	70	0.19	0.94	0.27	−11	−14	−7	−7	2.5	2.4 (1.8)	0.6	1.1 (1.2)
20	76	0.19	0.94	0.30	−13	−12	−8	−6	2.7	2.4 (1.7)	0.6	0.9 (1.2)
21	17	0.12	0.90	0.22	−14	−10	2	3	3.2	1.8 (1.5)	1.0	1.0 (1.3)
21	18	0.12	0.90	0.22	−17	−12	4	3	3.3	1.6 (1.5)	1.2	1.1 (1.3)
21	22	0.12	0.90	0.22	−18	−11	4	3	3.3	1.7 (1.5)	1.2	1.1 (1.3)
22	22	0.28	0.89	0.22	−34	−43	3	5	3.6	17.0 (7.7)	1.7	12.8 (6.4)
22	18	0.28	0.89	0.22	−37	−43	4	6	3.8	16.8 (7.9)	2.4	14.0 (6.6)
22	17	0.28	0.89	0.22	−50	−42	6	6	4.2	18.0 (8.0)	3.3	13.8 (6.9)
22	18	0.22	0.91	0.22	−38	−34	8	3	5.6	11.7 (5.8)	3.4	9.4 (5.0)
22	25	0.22	0.91	0.22	−37	−35	4	0	3.9	12.3 (5.8)	2.4	8.1 (4.8)
22	30	0.22	0.91	0.22	−43	−37	−1	−2	3.7	13.1 (5.7)	2.4	6.8 (4.7)
22	36	0.22	0.91	0.22	−41	−42	−4	−6	3.5	13.3 (5.6)	2.0	6.1 (4.6)
24	21	0.14	0.90	0.22	−23	−19	2	7	2.7	9.2 (2.7)	0.6	2.9 (2.6)
24	18	0.14	0.90	0.23	−24	−19	3	7	2.7	9.9 (2.8)	0.5	2.2 (2.6)
24	17	0.18	0.98	0.22	−21	−13	−4	−6	1.6	8.4 (3.2)	1.5	2.1 (3.0)
24	18	0.18	0.98	0.22	−7	−15	−3	−7	1.3	7.5 (3.2)	0.9	3.1 (2.9)
24	72	0.18	0.98	0.29	−5	−10	−3	−6	3.8	8.7 (4.3)	1.5	2.8 (2.6)
24	85	0.18	0.98	0.35	−5	−9	−5	−5	4.2	8.3 (4.1)	1.3	2.2 (2.0)

[a]O-TS indicates the DRF values simulated by the TS model by using optimized water vapor absorption coefficients and dust particle refractive indices. SZA represents the solar zenith angle. AOD and SSA indicate the aerosol optical depth at 440 nm and the single scattering albedo at 440 nm, respectively, from the AERONET Sun/sky photometer measurements. SA indicates the surface albedo obtained as the ratio of the upward SW flux to the downward SW flux, from the pyranometer measurements.

corresponding experimental values. In fact, the percentage value of the mean bias between simulated and experimental SW downward fluxes was −0.3% and +2.0% for GAME and the Two-Stream model, respectively. Analogously, GAME and the Two-Stream model on average underestimated by 1.5% and overestimated by 1.8% the corresponding SW upward fluxes measured at the surface. Note that the CMP 21 pyranometer has a total uncertainty of 2%, as outlined in section 2.2. Consequently, Figure 5 results support the good performance of both RTMs in the SW spectral range, being the mean bias percentage values within the experimental uncertainty of the pyranometer measurements. It is also worth noting that both models consider the spherical particle approximation to determine the radiative fluxes and *Kahnert et al.* [2007] found that the assumption of spherical particles in the simulation of SW downward fluxes implies errors between 5 and 10% for Saharan dust samples. However, one must be aware that desert particles monitored several thousand kilometers away from the sources may have undergone transformation processes and/or may have mixed with other particles such as anthropogenic particles during their transport to the monitoring site. Therefore, we can assume that desert particles monitored few thousand kilometers away from the source may have more regular shapes, according to *Chou et al.* [2008] and *Sicard et al.* [2014a]. Another possible source of discrepancy between the simulated and the experimental SW fluxes could be ascribed to the different spectral range of the measured and calculated flux values. In fact, the pyranometer measurements were performed in the 0.31–2.80 μm spectral range, while the GAME and Two-Stream fluxes were calculated in the range 0.3–4 μm.

Figures 6a and 6b show for comparison the LW calculated downward and upward fluxes, respectively, versus the corresponding measured fluxes at the surface. Black triangles and grey dots in Figure 6 represent the GAME and the Two-Stream calculated fluxes, respectively. Note that the measured LW radiative fluxes were also calculated by averaging the measured flux values over 10 min intervals centered at the selected times. Therefore, error bars in Figure 6 represent ±1 SD of the measured flux mean values. Observe from Figure 6 a that calculated GAME and Two-Stream LW downward fluxes on average slightly overestimated the corresponding experimental fluxes. In particular, the mean bias percentage was +1.6% and +1.3% for the GAME and the Two-Stream flux values, respectively. Note also from Figure 6a that the square of the linear

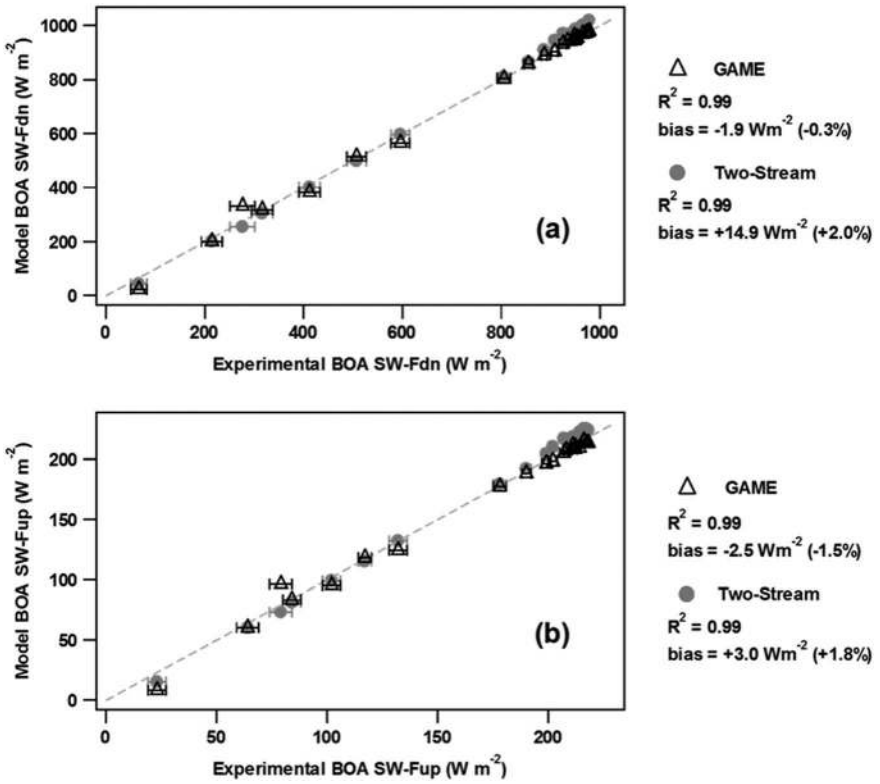

Figure 5. Comparison between experimental and simulated short-wave (a) downward and (b) upward radiative fluxes at the surface from 20 to 24 June 2013. Open black triangles and full grey dots represent the fluxes simulated by GAME and Two-Stream, respectively. Error bars represent the standard deviation of the measured radiative fluxes, which are obtained by averaging the related values within a 10 min interval centered at the selected time. The square of the linear correlation coefficient (R^2) and the mean bias are also reported. The grey dotted line represents the 1:1 line.

correlation coefficient between the GAME and the Two-Stream LW downward fluxes and the corresponding experimental fluxes was equal to 0.93 and 0.82, respectively. Figure 6b reveals that the agreement between the simulated and the measured LW upward fluxes was better than the one referring to the downward LW fluxes, being $R^2 = 0.99$ for the LW upward fluxes. In addition, Figure 6b reveals that on average the GAME and the Two-Stream LW upward fluxes overestimated by +0.2% and +0.04%, respectively, the corresponding fluxes measured at the surface. These last results were probably due to the strong dependence of the modeled LW upward fluxes at the BOA on the experimentally determined skin temperature (see equation (3)), which was retrieved from the pyrgeometers measurements and represented an input parameter for both RTMs. Note that the pyrgeometer's uncertainty is ±3% (section 2.2). Hence, Figure 6 reveals that the modeled LW fluxes at the surface also were in good agreement with the corresponding experimental fluxes. Note also that the pyrgeometers measurements were performed in the 4.5–42 μm spectral range, while the GAME and the Two-Stream LW fluxes were calculated in the 4–37 μm spectral range. Therefore, the different spectral range of the measured and calculated flux values could represent a possible source of discrepancy between the modeled and the experimental fluxes.

Figures 5 and 6 have revealed that the radiative flux values calculated by the two models were in good agreement with the corresponding experimental values. Hence, we believe that both figures have also indicated that the calculated SW and LW fluxes were not significantly affected by the different numerical procedure used by the two models to solve the radiative transfer equation, at least for the analysis performed in this study.

Figures 7a and 7b show by open boxes the Two-Stream upward fluxes at the top of the atmosphere (TOA) versus the corresponding GAME fluxes in the SW and LW range, respectively, to investigate the correlation between the TOA flux values provided by the two tested RTMs. Note that the TOA modeled fluxes could have been compared with corresponding satellite-based flux measurements, as the ones retrieved from CERES, to

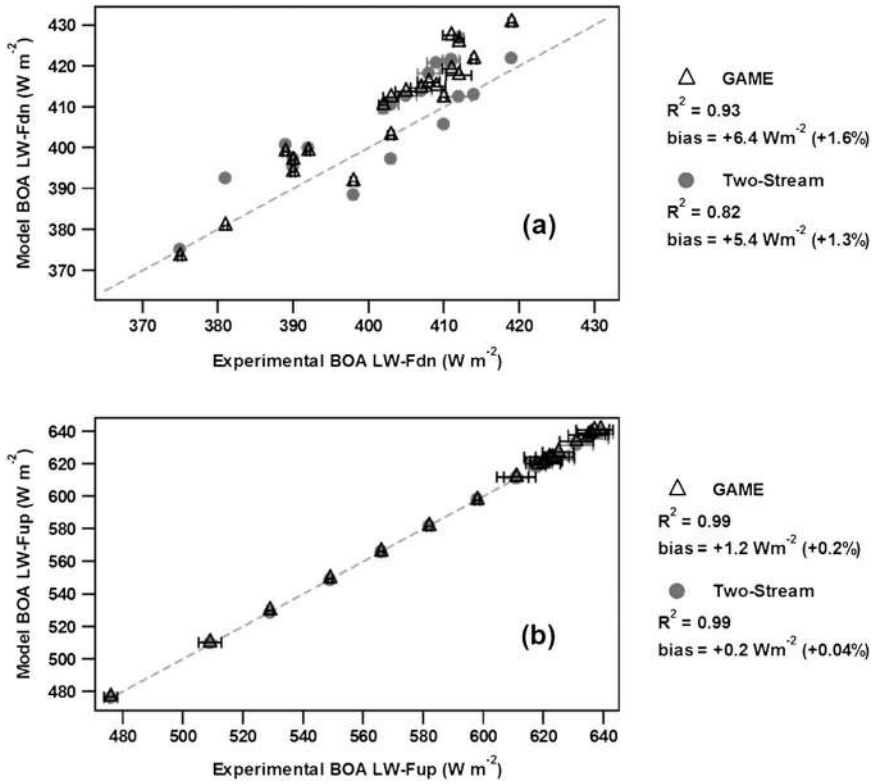

Figure 6. Comparison between experimental and simulated long-wave (a) downward and (b) upward radiative fluxes at the surface from 20 to 24 June 2013. Open black triangles and full grey dots represent the fluxes simulated by GAME and Two-Stream, respectively. Error bars represent the standard deviation of the measured radiative fluxes, which are obtained by averaging the related values within a 10 min interval centered at the selected time. The square of the linear correlation coefficient (R^2) and the mean bias are also reported. The grey dotted line represents the 1:1 line.

support/validate the GAME and the Two-Stream results at the TOA. We have not performed this comparison since for coastline areas, as the study site, CERES footprints contain information from both land and water. Consequently, we found large differences (up to 65% and 16% in the SW and in the LW range, respectively) between the CERES TOA fluxes and the simulated local 1-D flux estimations, mainly in the SW spectral range, because of the contribution of the sea surface albedo, according to *Sicard et al.* [2014a]. Note also that only four CERES measurements were collocated in space and time with the corresponding simulated fluxes during the analyzed Saharan dust event. Figures 7a and 7b reveal that the TOA Two-Stream upward fluxes were well correlated with the corresponding GAME fluxes in the SW ($R^2 = 0.99$) and LW ($R^2 = 0.96$) spectral range even if the Two-Stream upward fluxes overestimated the corresponding GAME fluxes: the mean bias percentage was of +9% and +6% in the SW and LW spectral ranges, respectively. The differences between GAME and Two-Stream TOA fluxes varied significantly with the monitoring day (not shown in Figure 7). Consequently, as it will be pointed out in the following section, we believe that the large bias values were mainly due to the poor spectral resolution of Two-Stream in comparison with GAME, in addition to the change of optical and microphysical properties of aerosol and water vapor, which represent the atmospheric components characterized by the highest day-to-day variability.

5.2. Aerosol Direct Radiative Forcing in Lecce During 20–24 June 2013

In this section, we present and analyze the model-based SW- and LW-DRF values calculated during the Saharan dust event that affected the central Mediterranean from 20 to 24 June 2013. Table 2 provides the instantaneous, clear-sky, and SW- and LW-DRF values both at the BOA and at the TOA calculated by GAME (G) and the Two-Stream (TS) RTM at different solar zenith angles (SZA) on 20–22, and 24 June, respectively. The corresponding AOD and SSA values at 440 nm and the surface albedo (SA) values have also been reported in Table 2. Figures 8a and 8c provide an overview of the temporal evolution of the BOA aerosol

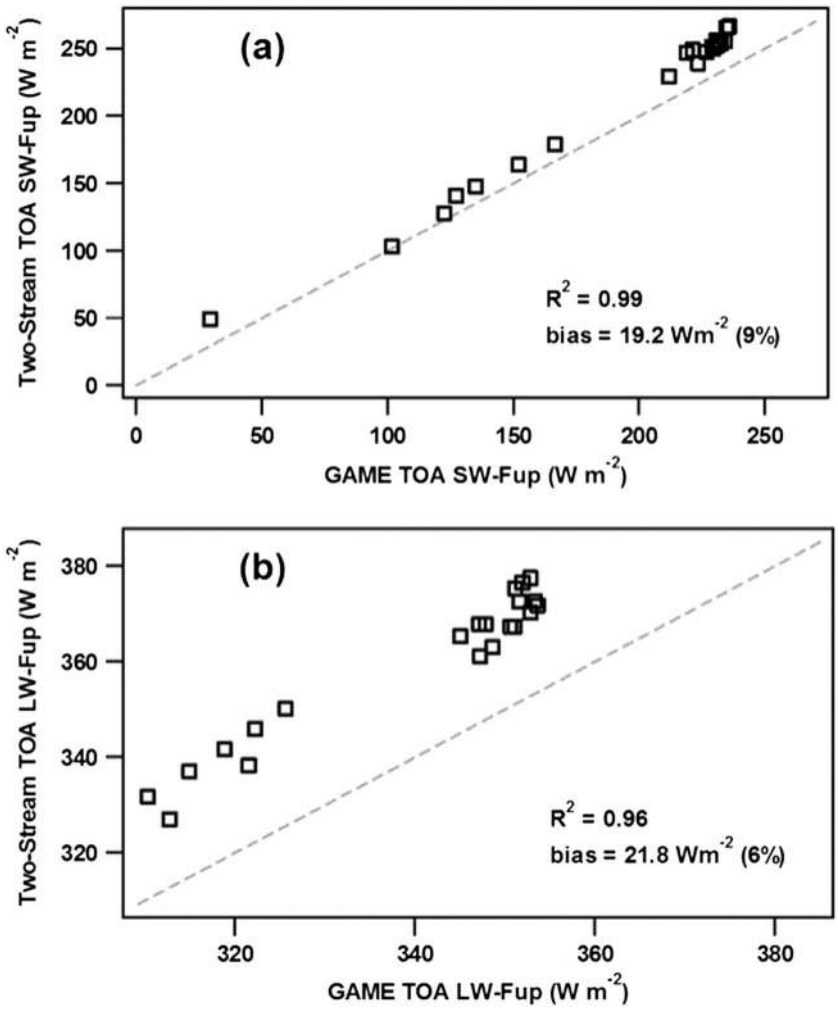

Figure 7. (a) Comparison between the upward radiative fluxes at the TOA simulated by GAME and Two-Stream in the (a) short- and (b) long-wave spectral ranges, from 20 to 24 June 2013. The square of the linear correlation coefficient (R^2) and the mean bias are also reported. The grey dotted line represents the 1:1 line.

SW- and LW-DRF, respectively, calculated by GAME (open black triangles) and the Two-Stream model (open grey dots), from 20 to 24 June 2013. No data were available on 23 June since it was a cloudy day and, consequently, AERONET Sun/sky photometer and lidar measurements were not performed. One observes from Table 2 and Figure 8a that at the BOA the GAME SW-DRFs varied from -5 to $-50\,W\,m^{-2}$, while the Two-Stream SW-DRF varied from -9 to $-43\,W\,m^{-2}$. Figure 8b shows the BOA SW-DRFs from the Two-Stream model versus the corresponding GAME values, and one observes that the Two-Stream data were well correlated with the corresponding GAME data ($R^2 = 0.86$) in the SW spectral range. The dashed grey line on Figure 8b represents the 1:1 line. The GAME LW-DRF at the surface ranged from +1.3 to $+5.6\,W\,m^{-2}$ (Table 2 and Figure 8c, open black triangles). Conversely, the corresponding Two-Stream LW-DRFs varied between +1.6 and $+18.0\,W\,m^{-2}$ (Table 2 and Figure 8c, open grey dots). Note that the BOA SW- and LW-DRFs are generally of opposite sign for desert dust. In fact, the scattering and absorption processes by aerosols cause the decrease of the incoming SW radiation at the surface, inducing a cooling effect and, hence, a negative value of the SW-DRF. Conversely, the scattering and absorption processes by desert aerosols in the LW spectral range enhance the greenhouse effect by trapping the outgoing LW radiation, and, hence, the LW-DRF is positive at the surface. Figure 8a reveals that the mean values of the modeled SW-DRF at the surface, which was equal to about $-13\,W\,m^{-2}$ on 21 June, decreased to about $-44\,W\,m^{-2}$ on 22 June because of the significant dust advection revealed by Figure 4. Then, Figure 8c shows that the BOA LW-DRF values determined by GAME, which were equal to about $+2.5\,W\,m^{-2}$ on 21 June, increased up to

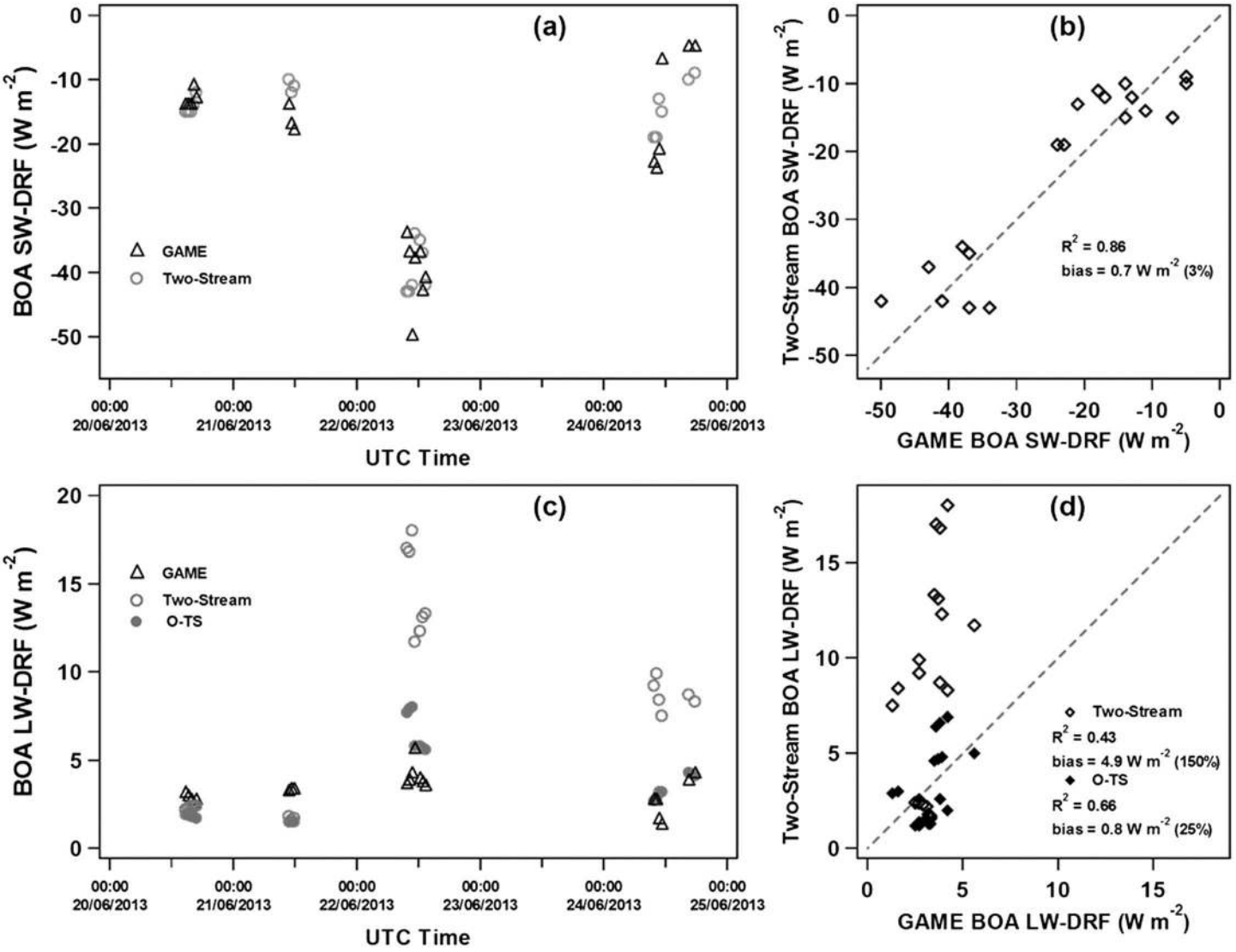

Figure 8. Temporal evolution of the (a) short- and (c) long-wave aerosol direct radiative forcing at the surface simulated by GAME (open black triangles) and Two-Stream (open grey dots) from 20 to 24 June 2013 in Lecce (Italy). The full grey dots in Figure 8c represent the long-wave aerosol direct radiative forcing at the surface obtained by using the optimized values of water vapor absorption coefficient and refractive index in the Two-Stream model, denoted as O-TS (Optimized Two-Stream). Comparison between the aerosol direct radiative forcing at the surface simulated by GAME and Two-Stream in the (b) short- and (d) long-wave ranges (open diamonds). Full diamonds in Figure 8d illustrate the comparison between the long-wave aerosol direct radiative forcing at the surface simulated by GAME and O-TS. The square of the linear correlation coefficient (R^2) and the mean bias are reported in Figures 8b and 8d. The grey dotted line represents the 1:1 line.

+5.6 W m^{-2} on 22 June. It is worth noting from Figure 8c and Table 2 that the LW-DRF values calculated from the Two-Stream model were significantly greater than the corresponding ones calculated from GAME on 22 and 24 June, which represented the days most affected by the Saharan dust intrusion (Figure 4). In particular, Figure 8d, which shows the BOA LW-DRFs from the Two-Stream model versus the GAME corresponding values, reveals that a poor correlation ($R^2 = 0.43$) and a quite large bias (+4.9 W m^{-2}) characterized the relationship between the two data sets. The LW-DRF values from the Two-Stream model referring to 22 and 24 June were mainly responsible for the poor correlation and large bias revealed from Figure 8d, as mentioned. Note that the BOA LW-DRFs by GAME and the TS model ranged from +2.5 to +3.3 W m^{-2} and from +1.6 to +2.4 W m^{-2}, respectively, on 20 and 21 June.

Figures 9a and 9c show the temporal evolution of the instantaneous, clear-sky and aerosol SW- and LW-DRF, respectively, at the TOA from 20 to 24 June 2013. Open black triangles and open grey dots represent the GAME and the Two-Stream simulated values, respectively. Figures 9b and 9d show the TOA SW- and

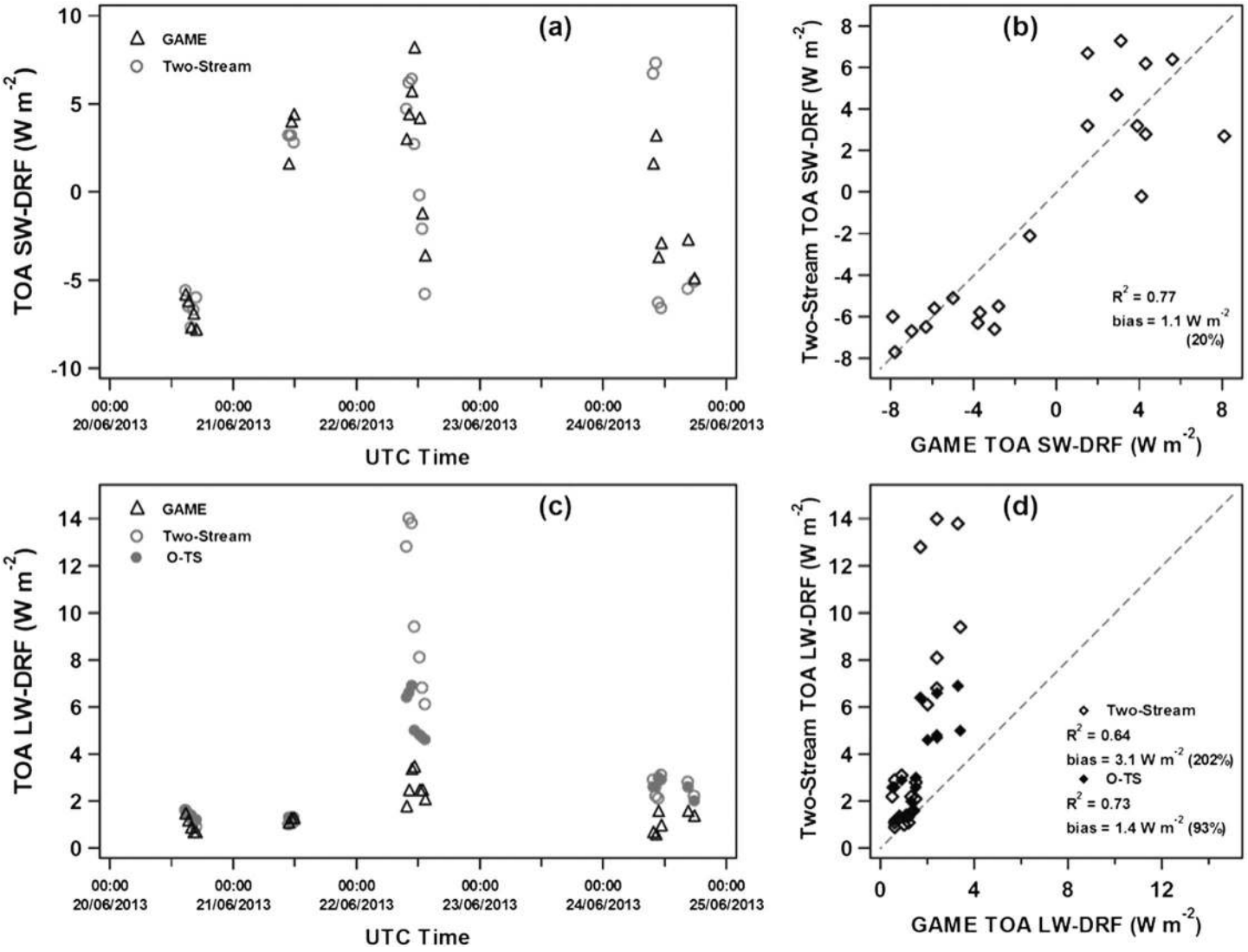

Figure 9. Temporal evolution of the (a) short- and (c) long-wave aerosol direct radiative forcing at the top of the atmosphere simulated by GAME (open black triangles) and Two-Stream (open grey dots) from 20 to 24 June 2013 in Lecce (Italy). The full grey dots in Figure 9c represent the long-wave aerosol direct radiative forcing at the TOA obtained by using the optimized values of water vapor absorption coefficient and refractive index in the Two-Stream model, denoted as O-TS (Optimized Two-Stream). Comparison between the aerosol direct radiative forcing at the TOA simulated by GAME and Two-Stream in the (b) short- and (d) long-wave ranges (open diamonds). Full diamonds in Figure 9d illustrate the comparison between the long-wave aerosol direct radiative forcing at the TOA simulated by GAME and O-TS. The square of the linear correlation coefficient (R^2) and the mean bias are reported in Figures 9b and 9d. The grey dotted line represents the 1:1 line.

LW-DRFs from the Two-Stream model, respectively, versus the corresponding GAME data. One observes that the TOA SW- and LW-DRFs from the Two-Stream model were relatively well correlated with the corresponding GAME data, being the square of the linear correlation coefficient equal to 0.77 and 0.64 for the SW (Figure 9b) and LW data set (Figure 9d), respectively. However, it is worth noting that on average the Two-Stream model overestimated the corresponding TOA DRFs from GAME. Consequently, the mean bias, which was equal to +1.1 W m^{-2} in the SW spectral range (Figure 9b), increased up to +3.1 W m^{-2} in the LW spectral range (Figure 9d). The results of Figures 8 and 9 reveal that the differences between the DRFs provided by the two models were on average larger in the LW spectral range. In particular, the largest differences were found at the TOA and at the surface on 22 June, which was the day characterized by the largest AODs (Figure 4a) and the smallest Ångström exponent values (Figure 4b) because of the large contribution of coarse particles. Figures 8c and 9c also reveal that the differences between the LW-DRF values from GAME and the Two-Stream model varied significantly with the monitoring day. Consequently, we believe that the optical and microphysical properties of aerosol and water vapor, which represent the atmospheric components

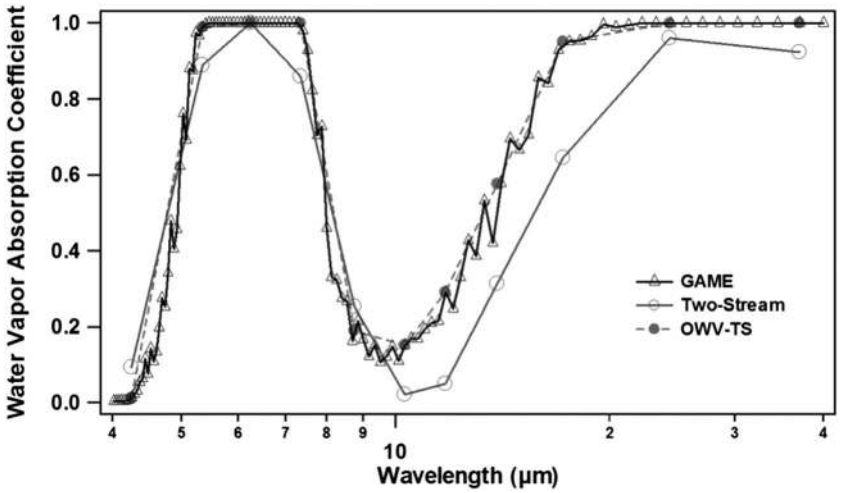

Figure 10. Water vapor absorption coefficient values (as a function of the wavelength, on logarithmic scale) used as input in the long-wave spectral range for GAME (open black triangles) and Two-Stream (open grey dots) related to the simulation at 09:47 UTC on 22 June 2013. The full grey dots represent the optimized water vapor profile for Two-Stream (OWV-TS) at the selected time.

characterized by the highest day-to-day variability, were likely responsible for the high bias values revealed from Figures 8d and 9d in the LW spectral range. The strong dependence on the monitoring day of the differences resulting from the LW-DRF estimates provided by the two models may also suggest that those differences were weakly or not affected by the different numerical procedure used by the two models to calculate the radiative field for a given distribution of aerosol and water vapor. The good agreement in the SW spectral range between the DRFs from the two models also supports the last statement. We believe that the poor spectral resolution of the Two-Stream model in the LW spectral range with respect to the one of GAME was likely responsible for the differences revealed from Figures 8c, 8d, 9c, and 9d, according to *Hatzianastassiou et al*. [2007]. The optimization procedures explained in the following and applied to both the water vapor absorption coefficient and the aerosol refractive index values in order to decrease the differences between the LW-DRF values calculated by GAME and the Two-Stream model will support this last statement.

5.2.1. Impact of the Water Vapor Absorption Coefficients on the LW Fluxes by the Two-Stream Model

A source of discrepancy in the radiative flux values and, consequently, in the DRF values provided by the two models could be due to the different spectroscopic database used by GAME and Two-Stream model for the atmospheric gases (HITRAN and LOWTRAN 5, respectively), as mentioned in section 3.3. In particular, the LOWTRAN 5 database may underestimate the near-infrared water vapor absorption by about 10%, according to *Halthore et al*. [2005]. Figure 10 shows, as an example, the water vapor absorption coefficient values as a function of the wavelength used by GAME (open black triangles) and Two-Stream (open grey dots) at 09:47 UTC on 22 June 2013 and clearly reveals the differences on the water vapor spectral absorption of the two models. Therefore, we decided to modify the water vapor absorption coefficients from the LOWTRAN 5 database at the 11 wavelengths that define the Two-Stream model resolution within the LW spectral range (4–37 μm, Table 1), to make the water vapor spectral absorption of the Two-Stream model closer to the one of GAME. The full grey dots in Figure 10 show the optimized water vapor (OWV) absorption spectrum at 09:47 UTC on 22 June 2013. The OWV absorption coefficient values were obtained by averaging the high spectral resolution GAME values in the corresponding Two-Stream LW subbands. The LW downward flux at the BOA and the LW upward flux at the TOA without aerosol (LW-$F^{DN,0}$ and -$F^{UP,0}$, respectively) have been simulated by using the OWV spectrum to evaluate its impact on the LW flux values. We found at 09:47 UTC on 22 June 2013 that the value of the BOA LW-$F^{DN,0}$ increased from 403.4 W m^{-2} up to 413.9 W m^{-2}, and, conversely, the value of the TOA LW-$F^{UP,0}$ decreased from 373.9 W m^{-2} up to 357.9 W m^{-2} by using the OWV absorption coefficient. The corresponding GAME values of the BOA LW-$F^{DN,0}$ and TOA LW-$F^{UP,0}$ were equal to 411.4 and 348.9 W m^{-2}, respectively. Therefore, the use of the OWV spectrum has allowed reducing the differences between the values of LW flux without aerosol provided by the two models up to 0.6% and

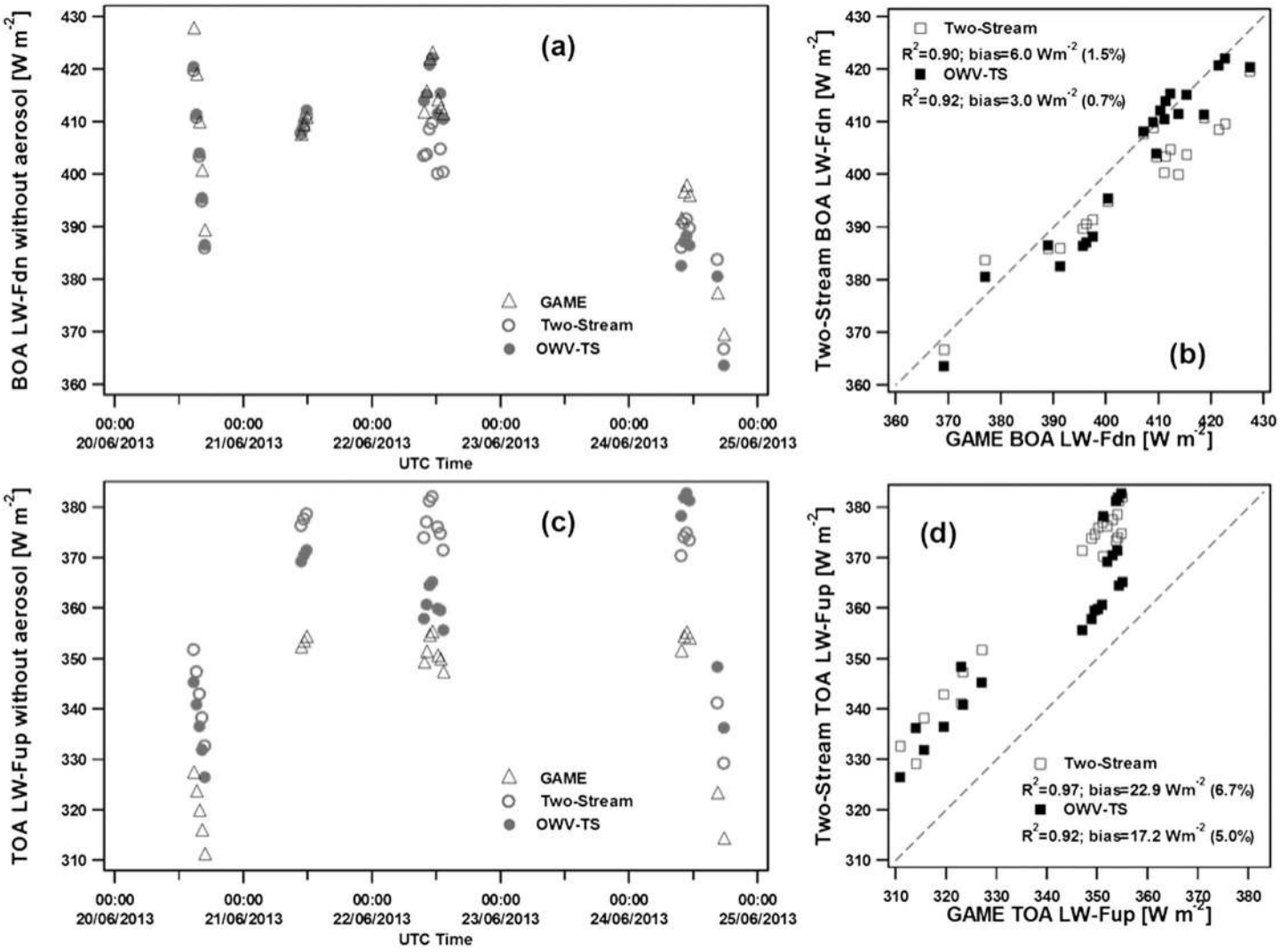

Figure 11. Temporal evolution of the LW (a) BOA downward and (c) TOA upward fluxes without aerosol simulated by GAME (open black triangles) and Two-Stream (open grey dots) in Lecce (Italy) for the period 20–24 June 2013. The full grey dots represent the LW (a) BOA downward and (c) TOA upward fluxes without aerosol simulated by Two-Stream with the optimized profile of the water vapor absorption (OWV-TS). LW (b) BOA downward and (d) TOA upward fluxes without aerosol simulated by the TS model (open boxes) and the OWV-TS model (full boxes) versus the corresponding GAME values. The square of the linear correlation coefficient (R^2) and the mean bias values are also reported. The grey dotted line represents the 1:1 line.

2.5% at the BOA and at the TOA, respectively. Figures 11a and 11c show the temporal evolution of the instantaneous BOA LW-$F^{DN,0}$ and TOA LW-$F^{UP,0}$ values, respectively, calculated by GAME (black open triangles) and the Two-Stream model (grey open dots), from 20 to 24 June 2013. Grey full dots in Figures 11a and 11c represent the instantaneous BOA LW-$F^{DN,0}$ and TOA LW-$F^{UP,0}$ values, respectively, calculated by using the OWV spectrum in the Two-Stream model, denoted as OWV-TS. Figures 11a and 11c reveal that the agreement between the flux values from GAME and the Two-Stream model on average improved by using the OWV spectral absorption. Figures 11b and 11d (open boxes) show the Two-Stream model instantaneous BOA LW-$F^{DN,0}$ and TOA LW-$F^{UP,0}$ values, respectively, versus the corresponding GAME values. Full boxes represent in Figures 11b and 11d the corresponding values of LW flux without aerosol calculated by using the OWV-TS model. The grey dashed line represents the 1:1 line in Figures 11b and 11d. One observes that the use of the OWV-TS has allowed improving the correlation and decreasing the mean bias between the BOA LW-$F^{DN,0}$ values provided by the two models (Figure 11b). This optimization has also allowed decreasing the mean bias between the TOA LW-$F^{UP,0}$ values simulated by the two tested models, as revealed by Figure 11d. Sensitivity tests revealed that the optimization of the water vapor absorption coefficients at 5.35, 6.25, and 7.35 μm was

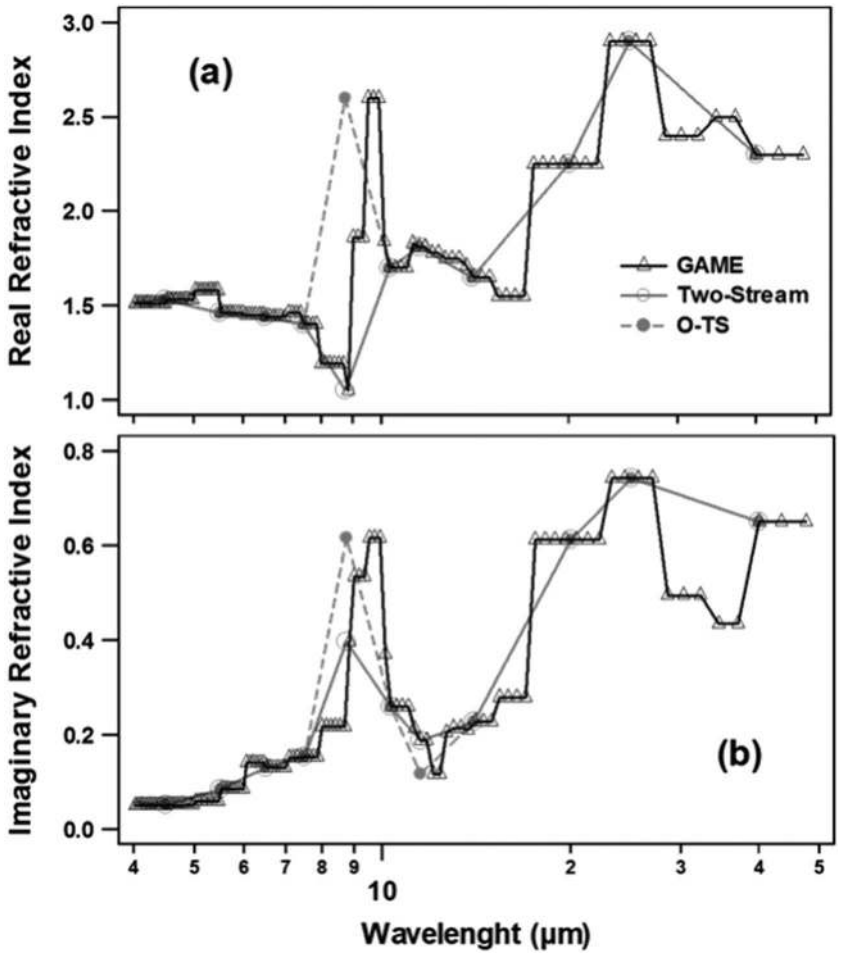

Figure 12. (a) Real and (b) imaginary refractive index values (as a function of the wavelength, on logarithmic scale) used as input in the long-wave spectral range for GAME (open black triangles) and Two-Stream (open grey dots). Full grey dots represent the optimized real (Figure 12a) and imaginary (Figure 12b) refractive index values used as input in the long-wave spectral range for Two-Stream (O-TS).

mainly responsible for the results of Figure 11. Note that the use of the OWV-TS model has also allowed decreasing the aerosol LW-DRF differences between the two tested models. In fact, sensitivity tests revealed that the use of the OWV absorption profile allowed decreasing by about 10% the differences between the aerosol LW-DRFs by GAME and the Two-Stream model, both at the BOA and at the TOA.

5.2.2. Impact of the Optimization of Refractive Index Values on the LW-DRFs by the Two-Stream Model

The time-independent refractive indices for mineral dust from *Krekov* [1993] were used in the LW spectral range by GAME and the Two-Stream model to calculate the aerosol DRF, as mentioned in section 3.3. Figure 12 shows the spectral dependence of the (a) real (*n*) and (b) imaginary (*k*) refractive index values in the LW spectral range. In particular, open triangles in Figures 12a and 12b show the *n* and *k* values, respectively, at the 115 LW subbands that characterize the GAME spectral resolution within the 4–37 μm spectral range (Table 1). To this end, one must be aware that *Krekov* [1993] provided the LW refractive index values in 27 spectral intervals. Grey open dots show the *n* and *k* values (Figures 12a and 12b, respectively) at the 11 LW subbands that characterize the Two-Stream model spectral resolution within the 4–37 μm spectral range (Table 1). Solid lines have been used to connect the data points and better visualize the *n* and *k* spectral dependence. Figures 12a and 12b reveal that the GAME *n* and *k* peak value at 9.5 μm was not accounted for in the Two-Stream model, because of its lower spectral resolution. Then, the Two-Stream *n* and *k* values at 8.75 μm have been set equal to 2.60 and 0.62, respectively, and the *k* value at 11.5 μm has been set equal to 0.12 to improve the agreement between the refractive index values used by the two models. Grey full dots in Figures 12a and 12b show the optimized *n* and *k* values, respectively. The aerosol LW-DRF has been

calculated with the Two-Stream model to evaluate the impact of the optimized values of n (at 8.75 μm) and k (at 8.75 and 11.5 μm). In fact, sensitivity tests revealed that the aerosol LW-DRF values were sensitive to changes of the refractive index values only within the 7.35–11.5 μm LW spectral range. In particular, we have found that the use of the optimized n and k values in the Two-Stream model allowed decreasing up to 80% the mean differences with the corresponding GAME LW-DRFs, both at the BOA and at the TOA. Therefore, the impact of the optimization of the refractive index values on the LW-DRF values was significantly larger than the one due to the optimization of the water vapor absorption profile (section 5.2.1).

Grey full dots in Figures 8c and 9c show the aerosol LW-DRFs at the surface and at the TOA, respectively, calculated with the Two-Stream model by taking into account both the OWV spectrum and the optimized n and k values at 8.75 and 11.5 μm, denoted as O-TS (Optimized Two-Stream). Figure 8d (full diamonds) shows the BOA LW-DRFs from the O-TS model versus the GAME corresponding values. One observes that the O-TS model has allowed increasing the square of the linear correlation coefficient (R^2) from 0.43 to 0.66 and decreasing the mean bias value from +4.9 to +0.8 W m^{-2}. Analogously, one can observe from Figure 9d that the O-TS model has also allowed improving the agreement with the TOA LW-DRFs from GAME, by increasing the R^2 value from 0.64 to 0.73 and decreasing the mean bias value from +3.1 to +1.4 W m^{-2}. Note that the impact of the O-TS model on the LW-DRF values was largest on 22 June, which represented the day most affected by desert dust. Therefore, Figures 8 and 9 have also highlighted that the LW spectral resolution impact on the aerosol LW-DRFs on average decreased with the decrease of the aerosol load and, more specifically, with the decrease of the coarse particle contribution. In fact, the LW radiation is mostly affected by coarse particles, such as sea salt and/or desert dust particles [*Sicard et al*., 2014b].

In conclusion, besides revealing the impact of spectrally averaged LW aerosol optical properties on aerosol DRF, the results of this section have also shown that the effects of a low spectral resolution in the radiative transfer (RT) calculations can be reduced by a suitable choice of the aerosol parameters at the available wavelengths. As previously reported, note that the optimization of the n and k values at 8.75 and 11.5 μm has allowed decreasing the mean aerosol LW-DRF by about 80%, both at the surface and at the TOA. *Hatzianastassiou et al*. [2007] evaluated the aerosol DRF within the 0.85–10 μm spectral range on a planetary scale by using both detailed spectral and spectrally averaged aerosol optical properties. They found that the use of spectrally averaged aerosol optical properties in the near-infrared spectral range, instead of detailed spectral ones, determined mostly an overestimation of the aerosol DRF both at the TOA and at the BOA, in accordance with the results of this study.

5.2.3. Comments on the Calculated SW- and LW-DRFs and Comparison With Previous Studies

Figure 9a shows the temporal evolution of the instantaneous and clear-sky values of the aerosol SW-DRF at the TOA calculated by GAME (black triangles) and the Two-Stream model (grey dots), from 20 to 24 June 2013. One observes that the calculated TOA SW-DRFs were negative on 20 June and positive on 21 June, while the two tested models provided both positive and negative TOA SW-DRFs on 22 and 24 June. A negative or positive sign of the aerosol DRF determines whether the aerosols produce a cooling or a heating effect [e.g., *Seinfeld and Pandis*, 1998]. The SSA, which measures the scattering versus absorption properties of an aerosol layer, represents the key parameter governing the amount of cooling versus heating. In fact, positive values of the aerosol DRF at the TOA reflect a strong absorption by the aerosol layer. Conversely, negative aerosol TOA DRFs indicate that the scattering processes by the aerosol particles predominate with respect to the absorption ones. However, one must be aware that for a given aerosol layer the critical SSA value (SSAc), which defines the boundary between cooling and heating, also depends on the surface albedo and the aerosol backscatter fraction (β) values [e.g., *Seinfeld and Pandis*, 1998, Figure 22.16]. In fact, the SSAc value on average increases with the increase of the surface albedo and the decrease of the aerosol backscatter fraction, for a given aerosol layer. Note that β increases with the solar zenith angle. Figures 13a–13c show the aerosol SW-DRF at the TOA calculated by GAME (open symbols) and the Two-Stream model (full symbols) versus the single scattering albedo at 440 nm, the experimentally determined surface albedo (SA), and the solar zenith angle, respectively, for 20 (dots), 21 (triangles), 22 (boxes), and 24 (diamonds) June 2013. One observes from Figure 13 that positive TOA SW-DRF values were associated with small values of SSA, SA, and SZAs, in agreement with the above comments. More specifically, one can estimate from Figure 13a that under our experimental conditions, the SSAc value was equal to 0.91 and was associated with SA values smaller than 0.225 (Figure 13b) and SZA values smaller than 25° (Figure 13c). Note that on 22 June positive and negative TOA SW-DRFs were provided by the two RTMs at SSA = 0.91 (Figure 13a, boxes). Figure 13c (boxes) reveals

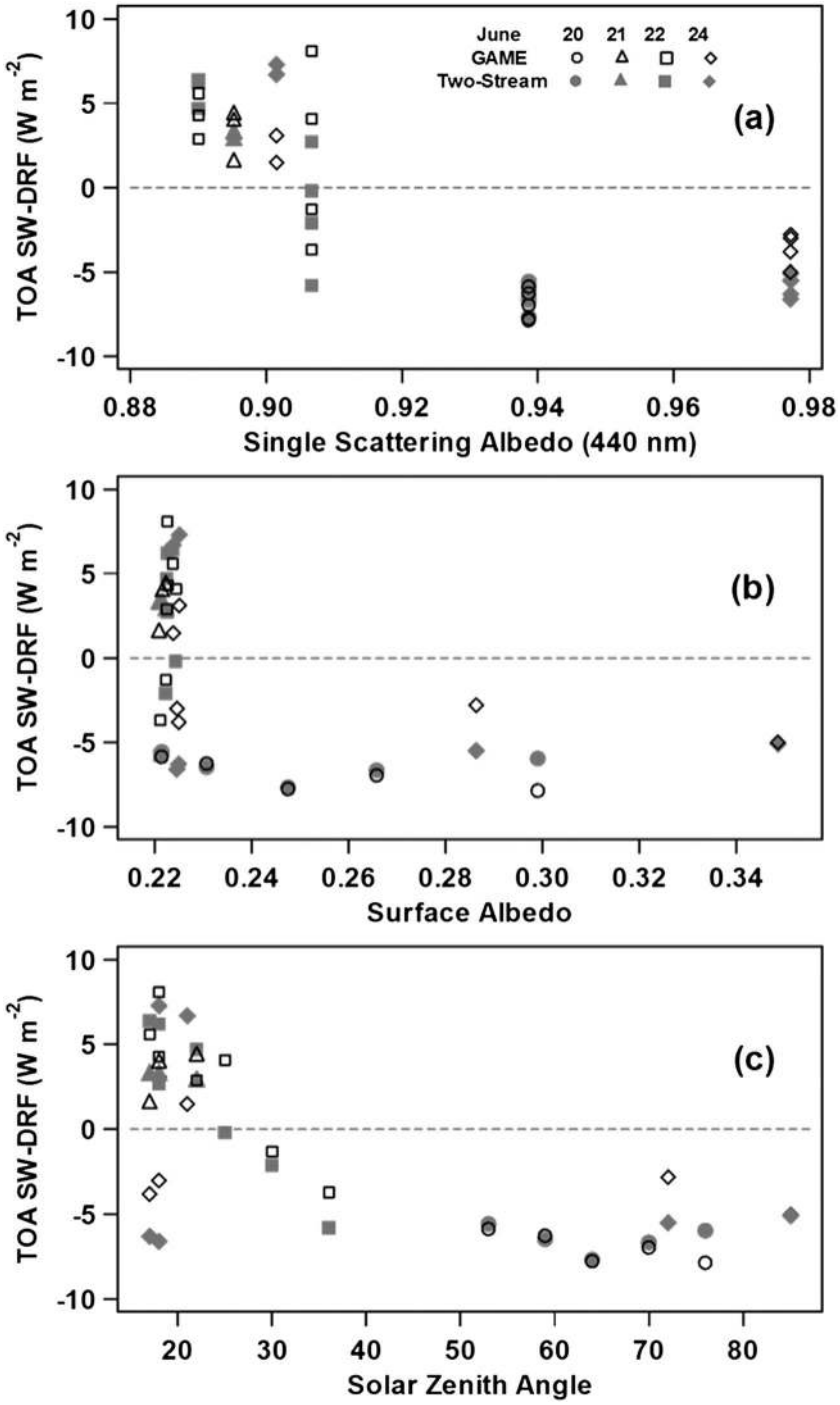

Figure 13. The instantaneous values of short-wave aerosol direct radiative forcing at the top of the atmosphere simulated by GAME (open black symbols) and Two-Stream (full grey symbols) for 20 (circles), 21 (triangles), 22 (boxes), and 24 (diamonds) June 2013 in Lecce (Italy) as a function of (a) single scattering albedo at 440 nm from AERONET Sun/sky photometer measurements, (b) surface albedo from pyranometers measurements, and (c) solar zenith angle. The dashed grey line represents TOA SW-DRF = 0 W m^{-2}.

that the negative TOA SW-DRFs were associated with SZAs greater than 29° and, hence, with greater back-scatter fraction values than the ones associated with SZAs smaller than 29°. *Sicard et al*. [2014a] calculated with GAME the instantaneous, clear-sky, TOA SW-DRF during 11 dust outbreaks, which affected Barcelona (Spain) from 2007 to 2012. They found that the TOA SW-DRF reached a positive value (+8.5 W m^{-2}) only

on 22 July 2009 for SSA (at 440 nm) = 0.83, SZA = 21.1°, and SA = 0.017. The low values of SSA, SZA, and SA were responsible for the positive value of the TOA SW-DRF, in agreement with the results of this study (Figure 13). In fact, *Sicard et al*. [2014a] found that the SSA (at 440 nm) reached a rather small value (0.79) also on 21 July 2009. Nevertheless, they found that the TOA SW-DRF value was negative ($-22.8\,W\,m^{-2}$) for SA = 0.017 and SZA = 77°. The larger SZA value was likely responsible for the negative sign of the TOA SW-DRF, according to Figure 13c. This last comment is supported by *Liao and Seinfeld* [1998], who have numerically investigated the TOA aerosol DRF for a uniform aerosol layer (from the Earth's surface to 5 km) made of pure ammonium sulfate, pure soot, internal mixture, and external mixture. They found at SZA = 0° that the aerosol SW-DRF was equal to -2.0 and $+5.5\,W\,m^{-2}$ for pure ammonium sulfate and soot, respectively, and that the internal and external mixtures were also responsible for positive TOA SW-DRFs ($+4.6\,W\,m^{-2}$ and $+3.6\,W\,m^{-2}$, respectively).

Figure 9a shows the temporal evolution of the instantaneous and clear-sky values of the aerosol SW-DRF at the TOA calculated by GAME (black triangles) and the Two-Stream model (grey dots), from 20 to 24 June 2013. One observes that the calculated TOA SW-DRFs were negative on 20 June and positive on 21 June, while the two tested models provided both positive and negative TOA SW-DRFs on 22 and 24 June. A negative or positive sign of the aerosol DRF determines whether the aerosols produce a cooling or a heating effect [e.g., *Seinfeld and Pandis*, 1998]. The SSA, which measures the scattering versus absorption properties of an aerosol layer, represents the key parameter governing the amount of cooling versus heating. In fact, positive values of the aerosol DRF at the TOA reflect a strong absorption by the aerosol layer. Conversely, negative aerosol TOA DRFs indicate that the scattering processes by the aerosol particles predominate with respect to the absorption ones. However, one must be aware that for a given aerosol layer the critical SSA value (SSAc), which defines the boundary between cooling and heating, also depends on the surface albedo and the aerosol backscatter fraction (β) values [e.g., *Seinfeld and Pandis*, 1998, Figure 22.16]. In fact, the SSAc value on average increases with the increase of the surface albedo and the decrease of the aerosol backscatter fraction, for a given aerosol layer. Note that β increases with the solar zenith angle. Figures 13a–13c show the aerosol SW-DRF at the TOA calculated by GAME (open symbols) and the Two-Stream model (full symbols) versus the single scattering albedo at 440 nm, the experimentally determined surface albedo (SA), and the solar zenith angle, respectively, for 20 (dots), 21 (triangles), 22 (boxes), and 24 (diamonds) June 2013. One observes from Figure 13 that positive TOA SW-DRF values were associated with small values of SSA, SA, and SZAs, in agreement with the above comments. More specifically, one can estimate from Figure 13a that under our experimental conditions, the SSAc value was equal to 0.91 and was associated with SA values smaller than 0.225 (Figure 13b) and SZA values smaller than 25° (Figure 13c). Note that on 22 June positive and negative TOA SW-DRFs were provided by the two RTMs at SSA = 0.91 (Figure 13a, boxes). Figure 13c (boxes) reveals that the negative TOA SW-DRFs were associated with SZAs greater than 29° and, hence, with greater backscatter fraction values than the ones associated with SZAs smaller than 29°. *Sicard et al*. [2014a] calculated with GAME the instantaneous, clear-sky, TOA SW-DRF during 11 dust outbreaks, which affected Barcelona (Spain) from 2007 to 2012. They found that the TOA SW-DRF reached a positive value ($+8.5\,W\,m^{-2}$) only on 22 July 2009 for SSA (at 440 nm) = 0.83, SZA = 21.1°, and SA = 0.017. The low values of SSA, SZA, and SA were responsible for the positive value of the TOA SW-DRF, in agreement with the results of this study (Figure 13). In fact, *Sicard et al*. [2014a] found that the SSA (at 440 nm) reached a rather small value (0.79) also on 21 July 2009. Nevertheless, they found that the TOA SW-DRF value was negative ($-22.8\,W\,m^{-2}$) for SA = 0.017 and SZA = 77°. The larger SZA value was likely responsible for the negative sign of the TOA SW-DRF, according to Figure 13c. This last comment is supported by *Liao and Seinfeld* [1998], who have numerically investigated the TOA aerosol DRF for a uniform aerosol layer (from the Earth's surface to 5 km) made of pure ammonium sulfate, pure soot, internal mixture, and external mixture. They found at SZA = 0° that the aerosol SW-DRF was equal to -2.0 and $+5.5\,W\,m^{-2}$ for pure ammonium sulfate and soot, respectively, and that the internal and external mixtures were also responsible for positive TOA SW-DRFs ($+4.6\,W\,m^{-2}$ and $+3.6\,W\,m^{-2}$, respectively).

Note from Figure 4c (black full triangles) that the SSA (at 440 nm) daily averaged value was smaller on 22 June than on 20 and 21 June. We believe that the small SSA values of 22 June were likely due to a mixing of desert dust with polluted particles. In fact, in a recent study, *Romano et al*. [2016] experimentally determined the BOA SW- and LW-DRF at the site of this study by using flux and AOD measurements, during the Saharan dust event that affected the central Mediterranean from 9 to 13 July 2012. In particular, they have shown that the

Two-Stream RTM could reproduce the experimental SW- and LW-DRFs at the surface by replacing the refractive indices typical of desert dust with the ones obtained for a mixture made of dust and soot particles. The dust contamination by anthropogenic particles during its transport to monitoring sites located a few thousand kilometers away from the source region was considered responsible for this last result. The low SSA values found by *Sicard et al*. [2014a] on 22 July 2009 and 21 June 2009 were also ascribed to the mixing of Saharan dust with pollution and biomass burning particles.

The BOA SW-DRFs of this study related to 22 June 2013 are in satisfactory agreement with the experimentally determined SW-DRFs at the surface reported by *Romano et al*. [2016] for 10 July 2012, which was a day characterized by aerosol properties similar to the one of this study. *Gómez-Amo et al*. [2011] have analyzed the instantaneous SW-DRF at Rome, Lecce, and Lampedusa, during the June 2007 Saharan dust event in the central Mediterranean by using the MODTRAN4 RTM. The three sites were considered representative for urban (Rome), suburban/rural (Lecce), and marine (Lampedusa) environments. The calculated SSA (at 416 nm) were smaller than the ones of this study at Lecce, likely as a consequence of a greater dust contamination by anthropogenic particles. In fact, the Rome SSA values were even smaller than the ones of Lecce, during the June 2007 Saharan dust event. Nevertheless, *Gómez-Amo et al*. [2011] found negative TOA SW-DRFs at SZA = 60° both at Rome and Lecce, in accordance with the above reported comments. It is also worth mentioning that the aerosol SW-DRFs of this study were both at the TOA and at the surface in good agreement with the ones reported by several authors and related to Mediterranean sites [e.g., *Perrone and Bergamo*, 2011; *Gómez-Amo et al*., 2011; *Perrone et al*., 2012; *Sicard et al*., 2014a, and references therein], if the SSA, AOD, SA, and SZA values are properly accounted for in the inter comparison analysis. Recently, *Mallet et al*. [2016] have reported some results on the aerosol radiation measurements and their modeling related to the ChArMEx/ADRIMED SOP-1a campaign, which took place from 11 June to 5 July 2013. Calculations of the 3-D (clear-sky) surface aerosol SW-DRF indicated an average from about -20 to $-10\,\mathrm{W\,m^{-2}}$ (for the whole period) over the Mediterranean Sea, together with maxima ($-50\,\mathrm{W\,m^{-2}}$) over northern Africa. The TOA aerosol DRF was shown to be highly variable within the domain, due to moderate absorbing properties of dust and changes in the surface albedo. Indeed, 3-D simulations indicated negative forcing over the Mediterranean Sea and Europe, and positive forcing over northern Africa. In particular, at Lampedusa the TOA SW-DRF values were at noon equal to about -7, -10, -15, and $-20\,\mathrm{W\,m^{-2}}$ on 20–22, and 24 June, respectively. They have ascribed the negative values of the TOA SW-DRF found at Lampedusa and all over the Mediterranean to the low SA values of the ADRIMED monitoring stations, since most of them were located over islands.

Several works have investigated the desert dust radiative impact mostly in the SW spectral range [e.g., *Gómez-Amo et al*., 2011, and references therein] over the Mediterranean area. Less attention was paid to the dust radiative impact in the LW spectral range, which is generally of opposite sign, as mentioned in section 5.2. Consequently, it is of peculiar importance to account for both the SW- and the LW-DRF to properly evaluate the desert dust role in the Earth's radiation budget. The results of this study revealed that the LW-DRF at the surface varied from +1.3 to $+5.6\,\mathrm{W\,m^{-2}}$ and from +1.5 to $+8.0\,\mathrm{W\,m^{-2}}$ for GAME and O-TS model, respectively. We have also found that the TOA LW-DRF ranged between +0.5 and $+3.4\,\mathrm{W\,m^{-2}}$ and between +1.2 and $+6.9\,\mathrm{W\,m^{-2}}$ for GAME and O-TS model, respectively. Results similar to the ones of this study were also reported by *Sicard et al*. [2014a], which evaluated with GAME the instantaneous and clear-sky LW-DRFs at the TOA and BOA during 11 desert dust outbreaks that occurred at Barcelona (Spain). In particular, they found that the TOA and BOA LW-DRF was equal to +2.1 and $+6.9\,\mathrm{W\,m^{-2}}$, respectively, on 21 May 2007 at SZA = 56.8° and to +0.6 and $+2.8\,\mathrm{W\,m^{-2}}$, respectively, on 12 April 2011 at SZA = 41°. *Romano et al*. [2016] estimated the instantaneous, clear-sky, aerosol TOA and BOA LW-DRF by the Two-Stream model at the study site, during the 9–13 July 2012 desert dust event, reporting values in satisfactory agreement with the ones of this study.

6. Summary and Conclusion

The instantaneous, clear-sky, aerosol DRFs in the SW and LW spectral range have been determined and analyzed in this study, within the ChArMEx/ADRIMED summer 2013 campaign. The aerosol DRFs at the TOA and at the surface have been calculated during the 20–24 June 2013 Saharan dust outbreak that affected southern Italy by using two RTMs (GAME and Two-Stream), characterized by different numerical methods to solve the RT equation and different spectral resolutions. Several relevant results were found:

1. The SW and LW radiative fluxes calculated by GAME and the Two-Stream RTM have firstly been compared with the corresponding radiative fluxes measured at the surface, to obtain a first estimate of the reliability of the data provided by the two tested RTMs. We have found a good agreement between modeled and experimental fluxes, both in the SW and in the LW range, within the experimental uncertainties of the measured flux values. Therefore, the validation of the modeled fluxes has not revealed any significant impact of the numerical method to solve the RT equation and the spectral resolution used by the two RTMs.
2. The GAME aerosol SW-DRFs at the BOA and at the TOA varied from -50 to $-5\,W\,m^{-2}$ and from -8 to $+8\,W\,m^{-2}$, respectively, in good agreement with the corresponding Two-Stream values, which ranged between -43 and $-9\,W\,m^{-2}$ at the BOA and -8 and $+7\,W\,m^{-2}$ at the TOA, during the investigated dust event.
3. We have also found that the two RTMs provided rather different LW-DRF values both at the TOA and at the BOA on the days significantly affected by desert dust. In particular, the Two-Stream model overestimated the GAME LW-DRF up to about 5 and 7.5 times at the surface and at the TOA, respectively, on 22 June, which was the day mostly affected by desert dust.
4. The strong dependence on the monitoring day of the differences associated with the LW-DRF values provided by the two models suggested that the spectrally averaged resolution of the Two-Stream model in the LW spectral range, to account for the aerosol properties and the water vapor absorption coefficients, was responsible for the LW-DRF overestimates by the Two-Stream model. In fact, aerosol and water vapor represent the atmospheric components characterized by the highest day-to-day variability.
5. It has been shown that the "optimization" of the water vapor absorption coefficients at the 11 subbands that characterize the LW spectral resolution of the Two-Stream model allowed decreasing the differences between the LW-DRFs calculated by the two models by about 10%, both at the BOA and at the TOA.
6. It has been shown that the low spectral resolution of the real (n) and imaginary (k) refractive index values was mainly responsible for the LW-DRF overestimates by the Two-Stream model. Then, we have demonstrated that the "optimization" of the n and k values at 8.75 and 11.5 μm was sufficient to obtain a satisfactory agreement between the LW-DRFs from the two models, both at the TOA and at the surface. In particular, we have found that the differences between the LW-DRF values determined by the two models decreased up to 80% because of the optimization of the refractive index values at 8.75 and 11.5 μm.
7. Negative and positive TOA SW-DRF values were found during the investigated Saharan dust outbreak. The positive TOA SW-DRF values were associated with low values of SSA, SA, and SZA. The dust contamination by anthropogenic particles during its transport to the monitoring site, which was located a few thousand kilometers away from the source region, was likely responsible for the increase of the light absorption by aerosol particles and, hence, for the decrease of the SSA values.

In conclusion, we believe that the results discussed in this paper can be considered of interest, since they have contributed to gain a better understanding of the model-based determination of the aerosol DRF associated with desert dust outbreaks over the Mediterranean basin.

Acknowledgments

S. Romano has carried out this work with the support of a PhD fellowship from the Mathematics and Physics Department of the Salento University. The financial support for EARLINET in the ACTRIS Research Infrastructure Project by the European Union's Horizon 2020 Research and Innovation Program under grant agreement 654169 and previously under grant agreement 262254 in the 7th Framework Program (FP7/2007–2013) is gratefully acknowledged. The intensive measurements in Lecce were performed in the framework of work package 4 on aerosol radiation-climate interactions of the coordinated program ChArMEx (the Chemistry-Aerosol Mediterranean Experiment; http://charmex.lsce.ipsl.fr). The color map of the aerosol optical depth (at 550 nm) daily mean values from the MSG-SEVIRI instrument were generated by ICARE Thematic Center (www.icare.univ.lille1.fr) and distributed by the ChArMEx operating center (http://choc.sedoo.fr/). The NOAA Air Resources Laboratory and Earth System Research Laboratory-Physical Science Division are kindly acknowledged for the provision of the HYSPLIT back trajectories and the geopotential height map, respectively. The radiative transfer calculations in Barcelona were supported by the Spanish Ministry of Economy and Competitivity (projects TEC2012-34575 and TEC2015-63832-P) and of Science and Innovation (project UNPC10-4E-442) and EFRD (European Fund for Regional Development); by the Department of Economy and Knowledge of the Catalan autonomous government (grant 2014 SGR 583). The authors kindly acknowledge Stefan Kinne for providing the Two-Stream radiative transfer model and Philippe Dubuisson for his valuable comments about the use and understanding of GAME model.

References

Anderson, G. P., S. A. Clough, F. X. Kneizys, J. H. Chetwynd, E. P. Shettle (1986), AFGL atmospheric constituent profiles (0–120 km), Rep. AFGL-TR-86-0110, Air Force Geophys. Lab., Hanscom Air Force Base, Mass.

Barragan, R., et al. (2015), Characterization of Saharan dust ageing over the western Mediterranean basin during a multi-intrusion event in June 2013 in the framework of the ADRIMED/ChArMEx campaign, Geophys. Res. Abstracts, vol. 17, EGU2015-2789, EGU General Assembly, Vienna, Austria, 12–17 April 2015.

Berk, A., et al. (2006), MODTRAN5: 2006 Update, Proc. SPIE, vol. 6233, 62331F.

Bilbao, J., and A. De Miguel (2007), Estimation of daylight downward longwave atmospheric irradiance under clear-sky and all-sky conditions, *J. Appl. Meteorol. Climatol.*, *46*, 878–889, doi:10.1175/JAM2503.1.

Bilbao, J., R. Román, C. Yousif, D. Mateos, and A. De Miguel (2014), Total ozone column, water vapour and aerosols effects on erythemal and global solar irradiance in Marsaxlokk, Malta, *Atmos. Environ.*, *99*, 508–518.

Cachorro, V. E., C. Toledano, N. Prats, M. Sorribas, S. Mogo, A. Berjón, B. Torres, R. Rodrigo, J. de la Rosa, and A. M. de Frutos (2008), The strongest desert dust intrusion mixed with smoke over the Iberian Peninsula registered with Sun photometry, *J. Geophys. Res.*, *113*, D14S04, doi:10.1029/2007JD009582.

Chou, C., P. Formenti, M. Maille, P. Ausset, G. Helas, M. Harrison, and S. Osborne (2008), Size distribution, shape, and composition of mineral dust aerosols collected during the African Monsoon Multidisciplinary Analysis Special Observation Period 0: Dust and Biomass-Burning Experiment field campaign in Niger, January 2006, *J. Geophys. Res.*, *113*, D00C10, doi:10.1029/2008JD009897.

De Tomasi, F., A. M. Tafuro, and M. R. Perrone (2006), Height and seasonal dependence of aerosol optical properties over southeast Italy, *J. Geophys. Res.*, *111*, D10203, doi:10.1029/2005JD006779.

Dubovik, O., A. Smirnov, B. N. Holben, M. D. King, Y. J. Kaufman, T. F. Eck, and I. Slutsker (2000), Accuracy assessment of aerosol optical properties retrieval from AERONET Sun and sky radiance measurements, *J. Geophys. Res.*, *105*, 9791–9806, doi:10.1029/2000JD900040.

Dubovik, O., B. N. Holben, T. Lapyonok, A. Sinyuk, M. I. Mishchenko, P. Yang, and I. Slutsker (2002), Non-spherical aerosol retrieval method employing light scattering by spheroids, *Geophys. Res. Lett.*, *10*(10), 1415, 10.1029/2001GL014506.

Dubovik, O., et al. (2006), Application of spheroid models to account for aerosol particle non-sphericity in remote sensing of desert dust, *J. Geophys. Res.*, *111*, D11208, doi:10.1029/2005JD006619.

Dubuisson, P., J. C. Buriez, and Y. Fouquart (1996), High spectral resolution solar radiative transfer in absorbing and scattering media: Application to the satellite simulation, *J. Quant. Spectrosc. Radiat. Transfer*, *55*, 103–126.

Dubuisson, P., D. Dessailly, M. Vesperini, and R. Frouin (2004), Water vapor retrieval over ocean using near-infrared radiometry, *J. Geophys. Res.*, *109*, D19106, doi:10.1029/2004JD004516.

Dubuisson, P., J. Roger, M. Mallet, and O. Dubovik (2006), A code to compute the direct solar radiative forcing: Application to anthropogenic aerosols during the Escompte Experiment, in *Proceedings International Radiation Symposium (IRS 2004) on Current Problems in Atmospheric Radiation*, edited by H. Fischer et al., pp. 127–130, A. Deepak, Busan, Korea.

Dulac, F. (2014), An overview of the Chemistry-Aerosol Mediterranean Experiment (ChArMEx), European Geosci. Union General Assembly, Geophys. Res. Abstracts vol. 16, EGU2014-11441, Vienna (Austria).

Formenti, P., et al. (2002), STAAARTE-MED 1998 summer airborne measurements over the Aegean Sea 2. Aerosol scattering and absorption, and 30 radiative calculations, *J. Geophys. Res.*, *107*(D21), 4451, doi:10.1029/2001JD001536.

Gómez-Amo, J. L., V. Pinti, T. Di Iorio, A. Di Sarra, D. Meloni, S. Becagli, V. Bellantone, M. Cacciani, D. Fuà, and M. R. Perrone (2011), The June 2007 Saharan dust event in the central Mediterranean: Observations and radiative effects in marine, urban, and sub-urban environments, *Atmos. Environ.*, *45*, 5385–5393.

Halthore, R. N., et al. (2005), Intercomparison of shortwave radiative transfer codes and measurements, *J. Geophys. Res.*, *110*, D11206, doi:10.1029/2004JD005293.

Hatzianastassiou, N., C. Matsoukas, A. Fotiadi, P. W. Stackhouse Jr., P. Koepke, K. G. Pavlakis, and I. Vardavas (2007), Modelling the direct effect of aerosols in the solar near-infrared on a planetary scale, *Atmos. Chem. Phys.*, *7*, 3211–3229.

Holben, B. N., et al. (1998), AERONET – A federated instrument network and data archive for aerosol characterization, *Remote Sens. Environ.*, *66*, 1–16.

Kahnert, M., T. Nousiainen, and P. Räisänen (2007), Mie simulations as an error source in mineral aerosol radiative forcing calculations, *Q. J. R. Meteorol. Soc.*, *133*, 299–307.

Key, J., and A. J. Schweiger (1998), Tools for atmospheric radiative transfer: Streamer and FluxNet, *Comp. Geosci.*, *24*, 443–451, doi:10.1016/S0098-3004(97)00130-1.

Krekov, G. M. (1993), Models of atmospheric aerosols, in *Aerosol Effects on Climate*, edited by S. G. Jennings, pp. 9–72, Univ. of Arizona Press, Tucson.

Larssen, S., R. Sluyter, C. Helmis (1999), Criteria for EUROAIRNET, the EEA Air Quality Monitoring and Information, Network. [Available at http://reports.eea.eu.int/TEC12/en.]

Lelieveld, J., et al. (2002), Global air pollution crossroads over the Mediterranean, *Science*, *298*, 794–799.

Liao, H., and J. Seinfeld (1998), Radiative forcing by mineral dust aerosols: Sensitivity to key variables, *J. Geophys. Res.*, *103*, 31,637–31,645, doi:10.1029/1998JD200036.

Mallet, M., V. Pont, C. Liousse, J. C. Roger, and P. Dubuisson (2006), Simulation of aerosol radiative properties with the ORISAM-RAD model during a pollution event (ESCOMPTE 2001), *Atmos. Environ.*, *40*, 7696–7705, doi:10.1016/j.atmosenv.2006.08.031.

Mallet, M., et al. (2016), Overview of the Chemistry-Aerosol Mediterranean Experiment/Aerosol Direct Radiative Forcing on the Mediterranean Climate (ChArMEx/ADRIMED) summer 2013 campaign, *Atmos. Chem. Phys.*, *16*, 455–504, doi:10.5194/acp-16-455-2016.

Manninen, T., A. Riihelä, and G. de Leeuw (2012), Atmospheric effect on the ground-based measurements of broadband surface albedo, *Atmos. Meas. Tech.*, *5*, 2675–2688, doi:10.5194/amt-5-2675-2012.

Mayer, B., and A. Kylling (2005), Technical note: The libRadtran software package for radiative transfer calculations – Description and examples of use, *Atmos. Chem. Phys.*, *5*, 1855–1877, doi:10.5194/acp-5-1855-2005.

Meador, W. E., and W. R. Weaver (1980), Two-stream approximation to radiative transfer in planetary atmospheres: A unified description of existing methods and new improvement, *J. Atmos. Sci.*, *37*, 630–643.

Meloni, D., A. Di Sarra, J. DeLuisi, T. Di Iorio, G. Fiocco, W. Junkermann, and G. Pace (2003), Tropospheric aerosols in the Mediterranean: 2. Radiative effects through model simulations and measurements, *J. Geophys. Res.*, *108*(D10), 4317, doi:10.1029/2002JD002807.

Meloni, D., W. Junkermann, A. di Sarra, M. Cacciani, L. De Silvestri, T. Di Iorio, V. Estellés, J. L. Gómez-Amo, G. Pace, and D. M. Sferlazzo (2015), Altitude-resolved shortwave and longwave radiative effects of desert dust in the Mediterranean during the GAMARF campaign: Indications of a net daily cooling in the dust layer, *J. Geophys. Res. Atmos.*, *120*, 3386–3407, doi:10.1002/2014JD022312.

Nabat, P., et al. (2015), Dust aerosol radiative effects during summer 2012 simulated with a coupled regional aerosol–atmosphere–ocean model over the Mediterranean, *Atmos. Chem. Phys.*, *15*, 3303–3326, doi:10.5194/acp-15-3303-2015.

Pappalardo, G., et al. (2014), EARLINET: Towards an advanced sustainable European aerosol lidar network, *Atmos. Meas. Tech.*, *7*, 2389–2409.

Perrone, M. R., and A. Bergamo (2011), Direct radiative forcing during Sahara dust intrusions at a site in the central Mediterranean: Anthropogenic particle contribution, *Atmos. Res.*, *101*, 783–798.

Perrone, M. R., A. M. Tafuro, and S. Kinne (2012), Dust layer effects on the atmospheric radiative budget and heating rate profiles, *Atmos. Environ.*, *59*, 344–354, doi:10.1016/j.atmosenv.2012.06.012.

Perrone, M. R., S. Romano, and J. A. G. Orza (2014a), Particle optical properties at a central Mediterranean site: Impact of advection routes and local meteorology, *Atmos. Res.*, *145–146*, 152–167, doi:10.1016/j.atmosres.2014.03.029.

Perrone, M. R., F. De Tomasi, and G. P. Gobbi (2014b), Vertically resolved aerosol properties by multi-wavelength lidar measurements, *Atmos. Chem. Phys.*, *14*, 1185–1204, doi:10.5194/acp-14-1185-2014.

Ricchiazzi, P., S. Yang, C. Gautier, and D. Sowle (1998), SBDART: A research and teaching software tool for plane-parallel radiative transfer in the Earth's atmosphere, *Bull. Am. Meteorol. Soc.*, *79*, 2101–2114, doi:10.1175/1520-0477(1998)079<2101:SARATS>2.0.CO;2.

Roger, J. C., M. Mallet, P. Dubuisson, H. Cachier, E. Vermote, O. Dubovik, and S. Despiau (2006), A synergetic approach for estimating the local direct aerosol forcing: Application to an urban zone during the Experience sur Site pour Contraindre les Modèles de Pollution et de Transport d'Emission (ESCOMPTE) experiment, *J. Geophys. Res.*, *111*, D13208, doi:10.1029/2005JD006361.

Román, R., M. Antón, A. Valenzuela, J. E. Gil, H. Lyamani, A. de Miguel, F. J. Olmo, J. Bilbao, and L. Alados-Arboledas (2013), Evaluation of the desert dust effects on global, direct and diffuse spectral ultraviolet irradiance, *Tellus B*, *65*, 19578, doi:10.3402/tellusb.v65i0.19578.

Romano, S., P. Burlizzi, and M. R. Perrone (2016), Experimental determination of short- and long-wave dust radiative effects in the central Mediterranean and comparison with model results, *Atmos. Res.*, *171*, 5–20, doi:10.1016/j.atmosres.2015.11.019.

Russell, P. B., R. W. Bergstrom, Y. Shinozuka, A. D. Clarke, P. F. De-Carlo, J. L. Jimenez, J. M. Livingston, J. Redemann, O. Dubovik, and A. Strawa (2010), Absorption Angstrom exponent in AERONET and related data as an indicator of aerosol composition, *Atmos. Chem. Phys.*, *10*, 1155–1169, doi:10.5194/acp-10-1155-2010.

Seinfeld J. H., and S. N. Pandis (1998), *Atmospheric Chemistry and Physics: From Air Pollution to Climate Change*, 1st ed., John Wiley, New York.

Sicard, M., M. Mallet, D. García-Vizcaíno, A. Comerón, F. Rocadenbosch, P. Dubuisson, and C. Muñoz-Porcar (2012), Intense dust and extremely fresh biomass burning in Barcelona, Spain: Characterization of their optical properties and estimation of their radiative forcing, *Environ. Res. Lett.*, *7*, 034016, doi:10.1088/1748-9326/7/3/034016.

Sicard, M., S. Bertolín, M. Mallet, P. Dubuisson, and A. Comerón (2014a), Estimation of mineral dust long-wave radiative forcing: Sensitivity study to particle properties and application to real cases in the region of Barcelona, *Atmos. Chem. Phys.*, *14*, 9213–9231, doi:10.5194/acp-14-9213-2014.

Sicard, M., S. Bertolín, C. Muñoz, A. Rodríguez, F. Rocadenbosch, and A. Comerón (2014b), Separation of aerosol fine- and coarse-mode radiative properties: Effect on the mineral dust longwave, direct radiative forcing, *Geophys. Res. Lett.*, *41*, 6978–6985, doi:10.1002/2014GL060946.

Sicard, M., R. Barragan, F. Dulac, L. Alados-Arboledas, and M. Mallet (2016), *Aerosol Optical, Microphysical and Radiative Properties at Regional Background Insular Sites in the Western Mediterranean basin*, Atmos. Chem. Phys. Discuss., doi:10.5194/acp-2015-823.

Stamnes, K., S. C. Tsay, W. Wiscombe, and K. Jayaweera (1988), Numerically stable algorithm for discrete-ordinate-method radiative transfer in multiple scattering and emitting layered media, *Appl. Opt.*, *27*(12), 2502–2509, doi:10.1364/AO.27.002502.

Stein, A. F., R. R. Draxler, G. D. Rolph, B. J. B. Stunder, M. D. Cohen, and F. Ngan (2015), NOAA's HYSPLIT atmospheric transport and dispersion modeling system, *Bull. Am. Meteorol. Soc.*, *96*, 2059–2077, doi:10.1175/BAMS-D-14-00110.1.

Tafuro, A. M., S. Kinne, F. De Tomasi, and M. R. Perrone (2007), Annual cycle of aerosol direct radiative effect over southeast Italy and sensitivity studies, *J. Geophys. Res.*, *112*, D20202, doi:10.1029/2006JD008265.

Valenzuela, A., F. J. Olmo, H. Lyamani, M. Antón, A. Quirantes, and L. Alados-Arboledas (2012), Aerosol radiative forcing during African desert dust events (2005–2010) over southeastern Spain, *Atmos. Chem. Phys.*, *12*, 10,331–10,351.

Wagner, W., and A. Pruß (2002), The IAPWS formulation 1995 for the thermodynamic properties of ordinary water substance for general and scientific use, *J. Phys. Chem. Ref. Data*, *31*, 387–535, doi:10.1063/1.1461829.

Wang, K., Z. Wan, P. Wang, M. Sparrow, J. Liu, X. Zhou, and S. Haginoya (2005), Estimation of surface long wave radiation and broadband emissivity using Moderate Resolution Imaging Spectroradiometer (MODIS) land surface temperature/emissivity products, *J. Geophys. Res.*, *110*, D11109, doi:10.1029/2004JD005566.

Yan, H., J. Huang, P. Minnis, T. Wang, and J. Bi (2011), Comparison of CERES surface radiation fluxes with surface observations over Loess Plateau, *Remote Sens. Environ.*, *115*, 1489–1500, doi:10.1016/j.rse.2011.02.008.